Dynamic Array-of-Subarrays Architecture for Wideband Multi-Antenna Systems

Seungnyun Kim, *Member, IEEE*, and Moe Z. Win, *Fellow, IEEE*

***Abstract*—Recently, wideband beamforming realized by extremely large-scale antenna array (ELAA) systems have garnered significant interest as a means to dramatically improve throughput of next generation (xG) networks. However, traditional phase shifter (PS)-based beamforming schemes might not work well in wideband ELAA systems due to the beam squint effect, where beams at different frequencies become misaligned. While the use of true time delay (TTD) can mitigate the beam squint effect by generating frequency-dependent beamforming vectors, the conventional TTD-based beamforming schemes suffer from significant array gain loss caused by the discrepancies between the desired directional beams and the generated beams. This beam misalignment issue becomes even more pronounced in the wideband ELAA systems due to the nonlinear near-field characteristics described by the spherical wave propagation. In this paper, we propose a wideband dynamic array-of-subarrays (WDAoSA) architecture that dynamically configures connections between TTDs and PS subarrays using a switch network. By optimizing the subarray connections as well as the TTD time delays and PS phase shifts, WDAoSA can effectively maximize the array gain of wideband ELAA systems. Numerical results demonstrate that WDAoSA achieves significant improvements in terms of array gain and spectral efficiency over the conventional TTD-based beamforming schemes.**

***Index Terms*—Wideband, beamforming, extremely large-scale antenna array, near-field, array-of-subarrays.**

I. Introduction

Wideband communications utilizing ELAA systems are key technologies of xG networks to support data-intensive applications such as digital twin, metaverse, and high-fidelity holograms [1], [2], [3], [4], [5], [6], [7]. Despite the extensive spectrum resources in millimeter-wave (mmWave) frequency range 2 (FR2) band (24-71 GHz) and sub-terahertz (THz) band (90-300 GHz), these high-frequency band signals suffer from significant attenuation caused by propagation loss, molecular absorption, and atmospheric attenuation [8], [9]. To compensate for the severe path loss, beamforming operation implemented by multi-antenna systems is essential [10], [11], [12], [13], [14], [15], [16], [17], [18], [19], [20], [21], [22], [23]. The main purpose of beamforming is to adjust the phase and amplitude of the transmit signal at each antenna so that the power of the signal received at user equipment (UE) is maximized. To do so, the beamforming vector should be properly aligned with the array steering vectors (set of phase delays for antenna elements) of the signal propagation paths [24], [25], [26], [27]. Traditionally, to adjust the phases of transmit signals, PSs that produce phase shifts invariant to the subcarrier frequency have been used extensively. The frequency-invariant beamforming techniques relying on PSs have been effective in conventional systems where the differences between subcarrier and carrier frequencies are negligible compared to the carrier frequency. However, they might not perform well in the wideband systems where the differences between the subcarrier and carrier frequencies are no longer negligible. Specifically, in the wideband systems, the array steering vectors are different for each subcarrier, meaning that the optimal beamforming vectors are dependent on the subcarrier frequencies [28], [29]. Due to this so-called *beam squint effect*, the conventional PS-based beamforming techniques suffer from severe degradation of array gain in the wideband ELAA systems.

To address the beam squint effect, frequency-dependent beamforming techniques that generate unique beamforming vectors for each subcarrier frequency are needed. The key component of the frequency-dependent beamforming is the TTD, a unit comprising multiple switched delay lines [30]. By choosing the delay line for the propagation of radio-frequency (RF) signals, a phase shift proportional to the product of the time delay and the signal frequency is induced to the incident RF signals. Recently, various TTD-based beamforming techniques have been proposed [31], [32], [33], [34], [35], [36], [37], [38]. In [31], a fully-connected TTD network employing TTDs equal to the number of transmit antennas has been proposed. While the TTD-based beamforming holds the potential to maximize the throughput, the use of micro-electromechanical systems (MEMS) based on expensive semiconductor lithographic processes for switching the delay lines in TTD results in high implementation costs [30]. To reduce hardware complexity and implementation cost of TTDs, in [32], [33], partially-connected hybrid networks with one TTD connected to multiple PSs have

Received 15 August 2024; revised 6 December 2024; accepted 20 January 2025. Date of current version 4 December 2025. The fundamental research described in this paper was supported, in part, by the National Research Foundation of Korea under Grant RS-2023-00252789, by the National Science Foundation under Grant CNS-2148251, by the federal agency and industry partners in the RINGS Program, and by the Robert R. Taylor Professorship. An earlier version of this paper was presented at the IEEE International Conference on Communications, Montreal, Canada, June 2025. The guest editor coordinating the review of this article and approving it for publication was Prof. Xiao Li. *(Corresponding author: Moe Z. Win.)*

Seungnyun Kim is with the Wireless Information and Network Sciences Laboratory, Massachusetts Institute of Technology, Cambridge, MA 02139 USA (e-mail: snkim94@mit.edu).

Moe Z. Win is with the Laboratory for Information and Decision Systems (LIDS), Massachusetts Institute of Technology, Cambridge, MA 02139 USA (e-mail: moewin@mit.edu).

Digital Object Identifier 10.1109/JSTSP.2025.3539208

been proposed. In [34], [35], TTD-based hybrid precoding techniques have been proposed. In [36], [37], wideband beamforming techniques for near-field systems have been proposed. Also, in [38], a dynamic subarray architecture with fixed time delays has been proposed.

While the conventional TTD-based beamforming techniques are effective to some extent, they may not perform well when the number of TTDs is relatively small compared to the number of antennas [33]. In such cases, these schemes fail to focus the directions of subcarrier beams on the UE, resulting in significant array gain degradation at the UE direction. Moreover, since the connections between the TTDs and the PS subarrays are fixed, a mismatch between the desired ultra-sharp pencil beams and the generated beams is unavoidable in the conventional TTD-based beamforming techniques. One exception is the dynamic subarray structure in [38], but in this scheme, the time delays of TTDs are fixed and not properly adjusted according to the wireless environments. The mismatch between the optimal beams and the generated beams of conventional TTD-based beamforming is even more serious in the wideband ELAA systems due to the near-field characteristics described by the nonlinear spherical wave propagation. The fundamental questions related to the wideband beamforming are: 1) how to configure the connections between TTDs and PS subarrays to maximize the array gain; and 2) how to control the time delays of TTDs and the phase shifts of PSs to maximize the throughput. The answers to these questions will lead to throughput maximization of the wideband ELAA systems via ultra-sharp pencil beamforming.

The primary purpose of this paper is to propose a new TTD-based beamforming architecture maximizing the array gain of wideband ELAA systems. The key ideas of the proposed scheme, henceforth referred to as *wideband dynamic array-of-subarrays* (WDAoSA), are twofold. First, WDAoSA dynamically configures the connections between TTDs and PS subarrays using a switch network. By properly choosing the TTDs to be connected to each PS subarray based on the wireless propagation environments, one can effectively bridge the gap between the desired ultra-sharp pencil beamforming vectors and the generated frequency-dependent beamforming vectors. Second, WDAoSA jointly optimizes the TTD time delays and the PS phase shifts. While the conventional TTD-based beamforming schemes design the beamforming vectors in forms of simple array steering vectors and thus, the degradation of array gain is unavoidable, such is not the case for WDAoSA since we deliberately optimize the TTD time delays and PS phase shifts to maximize the array gain.

The key contributions of this paper are as follows:

- we propose a wideband beamforming architecture where the connections between the TTDs and PS subarrays are dynamically adjusted to maximize the array gain;
- we develop both the centralized and distributed beamforming optimization algorithms for dynamic subarray connection and time delay and phase shift control; and
- we demonstrate from the extensive simulations that WDAoSA significantly improves the array gain over the conventional wideband beamforming schemes.

The rest of this paper is organized as follows. Section II discusses the wideband ELAA systems and reviews the conventional TTD-based beamforming schemes. Sections III and IV explain the network architecture of WDAoSA and propose the dynamic subarray connection and time delay/phase shift control algorithms. Section V analyzes the computational complexity of WDAoSA. Section VI presents the numerical results. Section VII concludes the paper.

Notation: Random variables are displayed in sans serif, upright fonts; their realizations in serif, italic fonts. Vectors and matrices are denoted by bold lowercase and uppercase letters, respectively. For example, a random variable and its realization are denoted by x and x for scalars, $\mathbf{\mathsf{x}}$ and $\boldsymbol{x}$ for vectors, and $\mathbf{\mathsf{X}}$ and $\boldsymbol{X}$ for matrices. Sets and random sets are denoted by upright sans serif and calligraphic font, respectively. For example, a random set and its realization are denoted by X and $\mathcal{X}$, respectively. The m-by-n matrix of zeros is denoted by $\mathbf{0}_{m\times n}$; when $n=1$, the m-dimensional vector of zeros is simply denoted by $\mathbf{0}_m$. The m-by-m identity matrix is denoted by $\boldsymbol{I}_m$. The operator $\|\boldsymbol{x}\|_2$ denotes the Euclidean norm. The operations $\otimes$ and $\odot$ denote the Kronecker product and element-wise product, respectively. The transpose, conjugate, and conjugate transpose of $\boldsymbol{X}$ are denoted by $(\cdot)^{\mathrm{T}}$, $(\cdot)^*$, and $(\cdot)^{\mathrm{H}}$, respectively. The real and imaginary parts of a complex number are denoted by $\Re\{\cdot\}$ and $\Im\{\cdot\}$, respectively. The notations $\mathrm{diag}(\boldsymbol{x})$ and $\boldsymbol{x}^{(p)}$ represent a diagonal matrix with the arguments being its diagonal elements and a vector with the pth power of arguments being its elements, respectively. The notation $\boldsymbol{e}_n$ is a unit vector whose nth element is 1 and all other elements are 0. The notation $\mathrm{supp}(\boldsymbol{x})$ denotes a vector of indices corresponding to the nonzero entries of $\boldsymbol{x}$. The nth element of $\boldsymbol{x}$ is denoted by $[\boldsymbol{x}]_n$. The notation $\boldsymbol{X}_{\boldsymbol{\pi}}$ represents a matrix whose ith column is the $\boldsymbol{\pi}(i)$th column of $\boldsymbol{X}$.

II. Wideband ELAA Systems

In this section, we explain wideband ELAA systems and spatial-wideband and beam squint effects. We then review conventional TTD-based beamforming schemes.

A. Downlink Wideband ELAA System Model

We consider a downlink wideband ELAA system where a base station (BS) equipped with $N = N_{\mathrm{h}} \times N_{\mathrm{v}}$ uniform rectangular array (URA) antennas serves a single-antenna UE. We assume that both the BS and UE have isotropic antenna arrays. The BS and UE are located at $\boldsymbol{p}^{\mathrm{bs}} \in \mathbb{R}^3$ and $\boldsymbol{p}^{\mathrm{ue}} \in \mathbb{R}^3$, respectively. Also, the nth BS antenna is located at $\boldsymbol{p}_n^{\mathrm{bs}} \in \mathbb{R}^3$.[1] We also consider an orthogonal frequency-division multiplexing (OFDM) system with the carrier frequency f_{c}, number of subcarriers S, and system bandwidth B. The BS is equipped with an analog beamforming architecture consisting of a single RF chain, T TTDs, and N PSs. The sets of indices for subcarrier, TTD, and PS are denoted as $\mathcal{S} \triangleq \{1, 2, \dots, S\}$, $\mathcal{T} \triangleq \{1, 2, \dots, T\}$, and $\mathcal{N} \triangleq \{1, 2, \dots, N\}$, respectively. The received signal $\mathsf{y}_s \in \mathbb{C}$

[1] Note that the BS antenna located at the xth row and yth column of the antenna array is referred to as the nth BS antenna where $n = (x-1)N_{\mathrm{v}} + y$.

of UE at the sth subcarrier is given by

$$\mathsf{y}_s = \sqrt{P_{\text{tx}}}\mathbf{h}_s^{\text{H}}\boldsymbol{w}_s\mathsf{x}_s + \mathsf{n}_s \tag{1}$$

where P_{tx} is the transmit power per subcarrier, $\mathbf{h}_s \in \mathbb{C}^N$ is the downlink channel vector, $\boldsymbol{w}_s \in \mathbb{C}^N$ is the analog beamforming vector such that $|[\boldsymbol{w}_s]_n| = 1$ for all $n \in \mathcal{N}$, $\mathsf{x}_s \sim \mathcal{CN}(0,1)$ is the data symbol, and $\mathsf{n}_s \sim \mathcal{CN}(0,\sigma^2)$ is the additive Gaussian noise. Then the spectral efficiency R of the UE is given by

$$\mathsf{R} = \frac{1}{S}\sum_{s=1}^{S}\log_2\left(1 + \frac{P_{\text{tx}}}{\sigma^2}\left|\mathbf{h}_s^{\text{H}}\boldsymbol{w}_s\right|^2\right). \tag{2}$$

In the wideband ELAA systems, due to the severe path loss and strong directivity of high-frequency band signals (e.g., mmWave FR2 and sub-THz bands), the signal power is concentrated on a few dominant paths [26]. Moreover, due to the extremely large number of antennas, the communication typically takes place in the near-field region where the signal wavefronts are modeled as spherical waves, rather than planar waves.[2] Based on these properties, we use the frequency-selective near-field channel model where the downlink channel frequency response (CFR) $\mathsf{h}_n(f) \in \mathbb{C}$ from the nth BS antenna to the UE can be obtained as

$$\mathsf{h}_n(f) = \sqrt{\beta(f)}\, e^{2\pi(f_{\text{c}}+f)\tau_n^{\text{los}}} + \sum_{i=1}^{N_{\text{p}}-1}\sqrt{\beta(f)}\,\alpha_i(f)\, e^{-2\pi(f_{\text{c}}+f)\tau_{n,i}} \tag{3}$$

where N_{p} is the number of propagation paths, and $\tau_n^{\text{los}} = \frac{\|\boldsymbol{p}^{\text{ue}}-\boldsymbol{p}_n^{\text{bs}}\|_2}{c}$ and $\tau_{n,i} = \frac{\|\boldsymbol{p}^{\text{ue}}-\boldsymbol{p}_i^{\text{sca}}\|_2}{c} + \frac{\|\boldsymbol{p}_i^{\text{sca}}-\boldsymbol{p}_n^{\text{bs}}\|_2}{c}$ are the time delays of the nth BS antenna for the line-of-sight (LoS) path and the ith non-line-of-sight (NLoS) path, respectively. Here, $\boldsymbol{p}_i^{\text{sca}} \in \mathbb{R}^3$ is the position vector of the ith NLoS scatterer and c is the speed of light. Also, $\beta(f) = (\frac{c}{4\pi(f_{\text{c}}+f)\|\boldsymbol{p}^{\text{ue}}-\boldsymbol{p}^{\text{bs}}\|_2})^2 e^{-k(f_{\text{c}}+f)\|\boldsymbol{p}^{\text{ue}}-\boldsymbol{p}_n^{\text{bs}}\|_2}$ is the path loss accounting for the free space path loss and the molecular absorption where $k(f_{\text{c}}+f)$ is the absorption coefficient [40], [41]. In addition, $\alpha_i(f) \sim \mathcal{CN}(0, \Gamma_i(f_{\text{c}}+f))$ is the path gain with $\Gamma_i(f_{\text{c}}+f)$ being the reflection coefficient [37], [42]. Due to the huge reflection loss at mmWave and THz bands, the power of the LoS component is typically -20 dB stronger than that of the NLoS component [26].

By collecting $\mathsf{h}_n(f)$ for all antenna elements $n \in \mathcal{N}$ and baseband frequency $\tilde{f}_s = \frac{B(s-1)}{S-1} - \frac{B}{2}$, we obtain the downlink channel vector $\mathbf{h}_s = [\,\mathsf{h}_1(\tilde{f}_s)\ \mathsf{h}_2(\tilde{f}_s)\ \cdots\ \mathsf{h}_N(\tilde{f}_s)\,]^{\text{T}} \in \mathbb{C}^N$ as

$$\mathbf{h}_s = \sqrt{\beta(f_s)}\,\boldsymbol{a}_N(\boldsymbol{p}^{\text{ue}}, f_s) + \sum_{i=1}^{N_{\text{p}}-1}\sqrt{\beta(f_s)}\,\tilde{\alpha}_i(f_s)\,\boldsymbol{a}_N(\boldsymbol{p}_i^{\text{sca}}, f_s) \tag{4}$$

where $f_s = f_{\text{c}} - \frac{B}{2} + \frac{B(s-1)}{S-1}$ is the sth subcarrier frequency, $\tilde{\alpha}_i(f_s) \triangleq \alpha_i(f_s)\, e^{j2\pi f_s \frac{\|\boldsymbol{p}^{\text{ue}}-\boldsymbol{p}_i^{\text{sca}}\|_2}{c}}$ is the effective path gain, and $\boldsymbol{a}_N(\boldsymbol{p}, f_s)$ is the $N \times 1$ near-field array steering vector at the sth subcarrier defined as

$$\boldsymbol{a}_N(\boldsymbol{p}, f_s) \triangleq \left[\, e^{-j2\pi f_s \frac{\|\boldsymbol{p}-\boldsymbol{p}_1^{\text{bs}}\|_2}{c}}\ e^{-j2\pi f_s \frac{\|\boldsymbol{p}-\boldsymbol{p}_2^{\text{bs}}\|_2}{c}}\ \cdots\ e^{-j2\pi f_s \frac{\|\boldsymbol{p}-\boldsymbol{p}_N^{\text{bs}}\|_2}{c}}\,\right]^{\text{T}}. \tag{5}$$

Then, the array gain $G(\boldsymbol{w}_s, \boldsymbol{p})$ of the sth subcarrier beamforming vector $\boldsymbol{w}_s$ at direction $\boldsymbol{p}$ is defined as

$$G(\boldsymbol{w}_s, \boldsymbol{p}) \triangleq \frac{1}{N}\boldsymbol{a}_N^{\text{H}}(\boldsymbol{p}, f_s)\,\boldsymbol{w}_s\,. \tag{6}$$

Also, the physical direction $\boldsymbol{\phi}(\boldsymbol{w}_s)$ of $\boldsymbol{w}_s$ is defined as

$$\boldsymbol{\phi}(\boldsymbol{w}_s) \triangleq \underset{\boldsymbol{p}\in\mathbb{R}^3}{\text{argmax}}\ |G(\boldsymbol{w}_s, \boldsymbol{p})|^2\,. \tag{7}$$

B. Spatial-Wideband and Beam Squint Effects in Wideband ELAA Systems

In traditional systems with relatively smaller antenna array and narrower bandwidth, the differences in time delays across antennas are negligible so the time delays are typically approximated as identical for all antennas, i.e., $\tau_{n,i} \approx \tau_i$. In wideband ELAA systems, however, the differences in time delays across the large antenna array become almost comparable to the sampling period [28], [29]. Due to this phenomenon, known as the *spatial-wideband effect*, distinct antenna elements may receive different transmit symbols [43].

In the frequency-domain, the spatial-wideband effect leads to frequency-dependent array steering vectors $\boldsymbol{a}_N(\boldsymbol{p}, f_s)$ (see (5)). (i.e., $\boldsymbol{a}_N(\boldsymbol{p}, f_i) \approx \boldsymbol{a}_N(\boldsymbol{p}, f_j)\ \forall i \neq j$). Since the beamforming vectors generated by PSs are identical across all subcarriers ($\boldsymbol{w}_i = \boldsymbol{w}_j\ \ \forall i \neq j$), the directions of the subcarrier beamforming vectors are distinct (i.e., $\boldsymbol{\phi}(\boldsymbol{w}_i) \neq \boldsymbol{\phi}(\boldsymbol{w}_j)\ \forall i \neq j$). This phenomenon where the direction of the subcarrier beam is dependent on the subcarrier frequency is called the *beam squint effect*. Since the subcarrier beamforming vectors are not aligned with the direction of UE, the conventional PS-based beamforming schemes suffer from severe array gain degradation in the wideband systems.[3]

C. Conventional TTD-Based Beamforming

To compensate for the throughput loss caused by the beam squint effect, beamforming approaches exploiting a combination of TTDs and PSs have been proposed [31], [32], [33], [34], [35], [36], [37], [38]. TTD is a device consisting of multiple switched delay lines. By choosing the delay line for the propagation of RF signals, a phase shift $e^{-j2\pi f_s\tau}$ proportional to the product of the time delay τ and the subcarrier frequency f_s is induced. Using multiple TTDs, one can generate frequency-dependent beamforming vectors. To be specific, the TTD beamforming

[2] In general, the electromagnetic (EM) radiation field can be divided into two regions: 1) the far-field region, where the EM radiation is approximated as plane waves; and 2) the near-field region, where the EM radiation is modeled as spherical waves. To distinguish these, the Fraunhofer distance $Z \triangleq \frac{N^2 c}{2 f_{\text{c}}}$ is widely used where c is the speed of light [39]. For example, in a mmWave ELAA system with $N = 512$ antennas operating at $f_{\text{c}} = 28$ GHz, Z is approximately 1.4 km, covering most of the microcell radius.

[3] In wideband systems, along with the spatial-wideband and beam squint effects, the grating lobes can also occur due to the mismatch between the fixed antenna spacing and varying half wavelengths of subcarrier signals [44].

vector $\boldsymbol{w}_s^{\mathrm{ttd}}(\boldsymbol{\tau}) \in \mathbb{C}^T$ at the sth subcarrier for given time delays $\boldsymbol{\tau} = [\,\tau_1\ \tau_2\ \cdots\ \tau_T\,]^{\mathrm{T}}$ of T TTDs is defined as

$$\boldsymbol{w}_s^{\mathrm{ttd}}(\boldsymbol{\tau}) \triangleq \left[\, e^{-j2\pi f_s \tau_1}\ e^{-j2\pi f_s \tau_2}\ \cdots\ e^{-j2\pi f_s \tau_T} \,\right]^{\mathrm{T}}. \tag{8}$$

Similarly, the PS beamforming vector $\boldsymbol{w}^{\mathrm{ps}}(\boldsymbol{\theta}) \in \mathbb{C}^N$ for given phase shifts $\boldsymbol{\theta} = [\,\theta_1\ \theta_2\ \cdots\ \theta_N\,]^{\mathrm{T}}$ of N PSs is defined as

$$\boldsymbol{w}^{\mathrm{ps}}(\boldsymbol{\theta}) \triangleq \left[\, e^{-j\theta_1}\ e^{-j\theta_2}\ \cdots\ e^{-j\theta_N} \,\right]^{\mathrm{T}}. \tag{9}$$

The conventional TTD-based beamforming schemes can be divided into two types: 1) fully-connected structure where each TTD is directly connected to the antenna ($T = N$); and 2) partially-connected structure where each TTD is connected to multiple PSs and then connected to the antenna ($T < N$).

1) Fully-Connected TTD-Based Beamforming: In the fully-connected structure, by employing a number of TTDs equal to the number of antennas, frequency-dependent beamforming vectors maximizing the array gain can be generated [31]. Specifically, for a given target direction $\boldsymbol{p}$, the time delays of N TTD are configured as

$$\boldsymbol{\tau}^{\mathrm{fc}} \triangleq \left[\, \frac{\|\boldsymbol{p}-\boldsymbol{p}_1^{\mathrm{bs}}\|_2}{c}\ \frac{\|\boldsymbol{p}-\boldsymbol{p}_2^{\mathrm{bs}}\|_2}{c}\ \cdots\ \frac{\|\boldsymbol{p}-\boldsymbol{p}_N^{\mathrm{bs}}\|_2}{c} \,\right]^{\mathrm{T}}. \tag{10}$$

Then the fully-connected beamforming vector $\boldsymbol{w}_s^{\mathrm{fc}} \in \mathbb{C}^N$ at the sth subcarrier is given by

$$\boldsymbol{w}_s^{\mathrm{fc}} \triangleq \boldsymbol{w}_s^{\mathrm{ttd}}(\boldsymbol{\tau}^{\mathrm{fc}}) = \boldsymbol{a}_N(\boldsymbol{p}, f_s)\,. \tag{11}$$

One can see that $\boldsymbol{w}_s^{\mathrm{fc}}$ achieves the maximum array gain of 1 as $\left|G(\boldsymbol{w}_s^{\mathrm{fc}}, \boldsymbol{p})\right| = \frac{1}{N}\left|\boldsymbol{a}_N^{\mathrm{H}}(\boldsymbol{p}, f_s)\,\boldsymbol{a}_N(\boldsymbol{p}, f_s)\right| = 1$.

2) Partially-Connected TTD-Based Beamforming: While the fully-connected structure can achieve the array gain maximization, the power consumption and implementation cost are considerable in the ELAA systems due to the large number of antennas. To reduce the power consumption and implementation cost, the partially-connected structures exploiting only a small number of TTDs have been proposed [32], [33], [34], [35], [36], [37], [38]. In the partially-connected structure, $T(< N)$ TTDs and N PSs are used where each TTD is connected to the PS subarray consisting of $P = \frac{N}{T}$ PSs. Specifically, the time delays of T TTDs and the phase shifts of N PSs are configured as

$$\boldsymbol{\tau}^{\mathrm{pc}} \triangleq \left[\, \frac{\|\boldsymbol{p}-\boldsymbol{p}_P^{\mathrm{bs}}\|_2}{c}\ \frac{\|\boldsymbol{p}-\boldsymbol{p}_{2P}^{\mathrm{bs}}\|_2}{c}\ \cdots\ \frac{\|\boldsymbol{p}-\boldsymbol{p}_{TP}^{\mathrm{bs}}\|_2}{c} \,\right]^{\mathrm{T}} \tag{12}$$

$$\boldsymbol{\theta}^{\mathrm{pc}} \triangleq 2\pi f_{\mathrm{c}} \left[\, \frac{\|\boldsymbol{p}-\boldsymbol{p}_1^{\mathrm{bs}}\|_2}{c}\ \frac{\|\boldsymbol{p}-\boldsymbol{p}_2^{\mathrm{bs}}\|_2}{c}\ \cdots\ \frac{\|\boldsymbol{p}-\boldsymbol{p}_N^{\mathrm{bs}}\|_2}{c} \,\right]^{\mathrm{T}} - (2\pi f_{\mathrm{c}} \boldsymbol{\tau}^{\mathrm{pc}}) \otimes \mathbf{1}_P\,. \tag{13}$$

By plugging $\boldsymbol{\tau}^{\mathrm{pc}}$ and $\boldsymbol{\theta}^{\mathrm{pc}}$ to (8) and (9), the corresponding TTD and PS beamforming vectors are given by

$$\boldsymbol{w}_s^{\mathrm{ttd}}(\boldsymbol{\tau}^{\mathrm{pc}}) = \left[[\boldsymbol{a}_N(\boldsymbol{p}, f_s)]_{tP}\ :\ t = 1, 2, \ldots, T\right]^{\mathrm{T}} \tag{14}$$

$$\boldsymbol{w}^{\mathrm{ps}}(\boldsymbol{\theta}^{\mathrm{pc}}) = \boldsymbol{a}_N(\boldsymbol{p}, f_{\mathrm{c}}) \odot \left(\left[[\boldsymbol{a}_N(\boldsymbol{p}, f_{\mathrm{c}})]_{tP}^{-1}\ :\ t = 1, 2, \ldots, T\right]^{\mathrm{T}} \otimes \mathbf{1}_P\right). \tag{15}$$

Then, the partially-connected beamforming vector $\boldsymbol{w}_s^{\mathrm{pc}} \in \mathbb{C}^N$ at the sth subcarrier is given by

$$\boldsymbol{w}_s^{\mathrm{pc}} \triangleq \boldsymbol{w}^{\mathrm{ps}}(\boldsymbol{\theta}^{\mathrm{pc}}) \odot \left(\boldsymbol{w}_s^{\mathrm{ttd}}(\boldsymbol{\tau}^{\mathrm{pc}}) \otimes \mathbf{1}_P\right) \tag{16}$$

$$= \boldsymbol{a}_N(\boldsymbol{p}, f_{\mathrm{c}}) \odot \left(\left[\frac{[\boldsymbol{a}_N(\boldsymbol{p}, f_s)]_{tP}}{[\boldsymbol{a}_N(\boldsymbol{p}, f_{\mathrm{c}})]_{tP}}\ :\ t = 1, 2, \ldots, T\right]^{\mathrm{T}} \otimes \mathbf{1}_P\right). \tag{17}$$

One can see that when $f_s = f_{\mathrm{c}}$, we have $\boldsymbol{w}_s^{\mathrm{pc}} = \boldsymbol{w}_s^{\mathrm{fc}}$ but this equality does not hold when $f_s \neq f_{\mathrm{c}}$. This mismatch causes a degradation in both the array gain $G(\boldsymbol{w}_s, \boldsymbol{p})$ and the spectral efficiency R. In fact, the mismatch between $\boldsymbol{w}_s^{\mathrm{pc}}$ and $\boldsymbol{w}_s^{\mathrm{fc}}$ becomes more pronounced as $|f_s - f_{\mathrm{c}}|$ increases, leading to significant array gain losses in the subcarrier beams.

III. Wideband Dynamic Array-of-Subarray Architecture: Centralized Approach

The main goal of the proposed WDAoSA is to generate beamforming vectors directed toward a target direction while maximizing the array gain using a small number of TTDs.[4] Recall that conventional partially-connected structure suffers from significant array gain degradation due to the fixed connections between TTDs and PS subarrays. To handle this issue, WDAoSA exploits a switch network that dynamically configures the subarray connection as well as the TTD time delays and PS phase shifts to maximize the array gain.

A. WDAoSA Network Architecture

The proposed WDAoSA consists of three major components: 1) a TTD network with T TTDs; 2) a switch network; and 3) a PS network with N PSs (see Fig. 1). The N PSs are divided into L subarrays, each consisting of $\frac{N}{L} = K$ PSs and a single-pole multiple-throw (SPMT) switch that can be connected to one of TTDs. The set of $TTDs$ and PS subarrays are denoted as $\mathcal{T} \triangleq \{1, 2, \ldots, T\}$ and $\mathcal{L} \triangleq \{1, 2, \ldots, L\}$. Let $\pi_l \in \mathcal{T}$ be the index of TTD connected to the lth PS subarray and $\boldsymbol{\pi} \in \mathcal{T}^L$ be the subarray connection vector defined as

$$\boldsymbol{\pi} \triangleq [\,\pi_1\ \pi_2\ \cdots\ \pi_L\,]^{\mathrm{T}}. \tag{18}$$

Also, let τ_t and θ_n be the time delay and the phase shift of the tth TTD and the nth PS, respectively and $\boldsymbol{\tau} \in \mathbb{R}^T$ and $\boldsymbol{\theta} \in \mathbb{R}^N$ be the time delay and phase shift vectors defined as

$$\boldsymbol{\tau} \triangleq [\,\tau_1\ \tau_2\ \cdots\ \tau_T\,]^{\mathrm{T}} \tag{19}$$

$$\boldsymbol{\theta} \triangleq [\,\theta_1\ \theta_2\ \cdots\ \theta_N\,]^{\mathrm{T}}. \tag{20}$$

Then, the WDAoSA beamforming vector $\boldsymbol{w}_s \in \mathbb{C}^N$ at the sth subcarrier is defined as a function of $\boldsymbol{\pi}$, $\boldsymbol{\tau}$, and $\boldsymbol{\theta}$ as

$$\boldsymbol{w}_s \triangleq \boldsymbol{w}^{\mathrm{ps}}(\boldsymbol{\theta}) \odot \left(\left(\boldsymbol{E}_{\boldsymbol{\pi}}^{\mathrm{T}} \boldsymbol{w}_s^{\mathrm{ttd}}(\boldsymbol{\tau})\right) \otimes \mathbf{1}_K\right) \tag{21}$$

where $\boldsymbol{w}_s^{\mathrm{ttd}}(\boldsymbol{\tau})$ and $\boldsymbol{w}^{\mathrm{ps}}(\boldsymbol{\theta})$ are the TTD and PS beamforming vectors defined in (8) and (9), respectively. Also, $\boldsymbol{E}_{\boldsymbol{\pi}} \in \mathbb{R}^{T \times L}$ is the subarray connection matrix defined as

$$\boldsymbol{E}_{\boldsymbol{\pi}} \triangleq [\,\boldsymbol{e}_{\pi_1}\ \boldsymbol{e}_{\pi_2}\ \cdots\ \boldsymbol{e}_{\pi_L}\,] \tag{22}$$

where $\boldsymbol{e}_{\pi_l}$ is a $T \times 1$ vector whose π_lth element is 1 and all other elements are 0. When comparing the WDAoSA beamforming

[4]By generating multiple sets of beamforming vectors directed toward a range of different directions, we can construct a beam codebook for the beam sweeping operation in 5G New Radio (NR) beam management [45], [46].

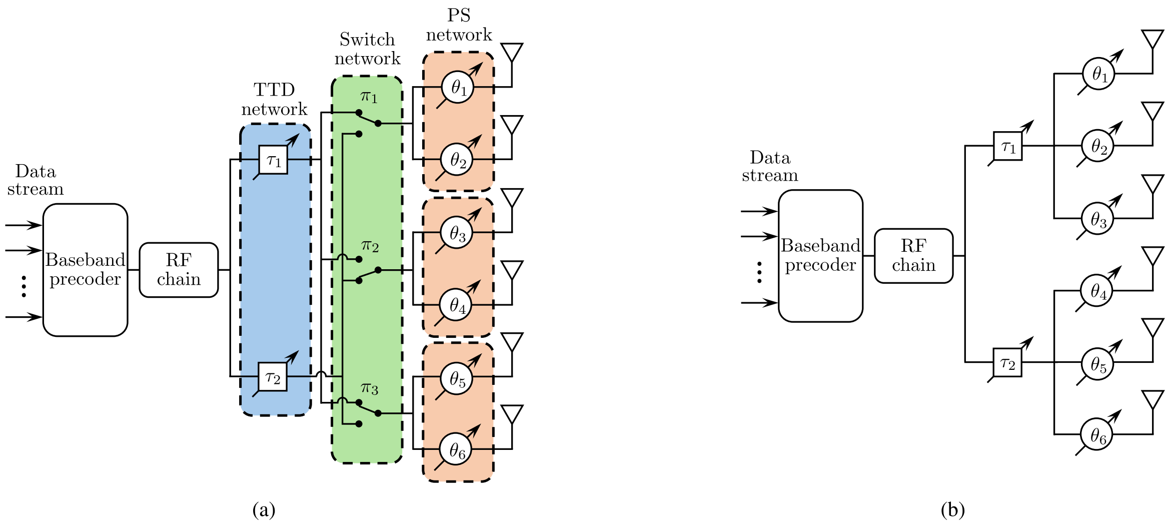

Fig. 1. Comparison between (a) the proposed WDAoSA scheme and (b) the conventional TTD-based beamforming scheme.

vector $\boldsymbol{w}_s$ in (21) with the conventional partially-connected beamforming vector $\boldsymbol{w}_s^{\text{pc}}$ in (17), two major differences stand out: 1) the subarray connection matrix $\boldsymbol{E}_{\boldsymbol{\pi}}$ is multiplied by $\boldsymbol{w}_s^{\text{ttd}}(\boldsymbol{\tau})$ to dynamically adjust the connection between TTDs and PS subarrays; and 2) the time delays $\boldsymbol{\tau}$ and phase shifts $\boldsymbol{\theta}$ are optimized to maximize the array gain.

Now we formulate the wideband beamforming optimization problem to determine $(\boldsymbol{\pi}, \boldsymbol{\tau}, \boldsymbol{\theta})$ maximizing the array gain at the target direction $\boldsymbol{p}$. However, this task is not straightforward since the array gains $\{G(\boldsymbol{w}_s, \boldsymbol{p})\}_{s=1}^S$ of all subcarriers must be considered simultaneously. To address this issue, we exploit the fact that R is a sum of logarithms of channel gains. Specifically, we define the total array gain $G_{\text{tot}}(\{\boldsymbol{w}_s\}_{s=1}^S, \boldsymbol{p})$:

$$G_{\text{tot}}\left(\{\boldsymbol{w}_s\}_{s=1}^S, \boldsymbol{p}\right) \triangleq \sum_{s=1}^{S} \log_2\left(1 + \rho_s |G(\boldsymbol{w}_s, \boldsymbol{p})|^2\right) \tag{24}$$

where $\rho_s \triangleq \frac{\beta(f_s) N P_{\text{tx}}}{\sigma^2}$ is the signal-to-noise ratio (SNR) at the sth subcarrier. Note that G_{tot} becomes the same as R when $\boldsymbol{p}^{\text{ue}} = \boldsymbol{p}$ and $\mathbf{h}_s$ has only the LoS component. By employing G_{tot} as the objective function in the wideband beamforming optimization, we can guide the WDAoSA beam generation to maximize the spectral efficiency without relying on the explicit channel information $\{\mathbf{h}_s\}_{s=1}^S$. The wideband beamforming optimization problem $\mathscr{P}_0$ is formulated as

$$\mathscr{P}_0 : \quad \underset{\boldsymbol{\pi}, \boldsymbol{\tau}, \boldsymbol{\theta}}{\text{maximize}} \quad \sum_{s=1}^{S} \log_2\left(1 + \frac{\rho_s}{N^2}\left|\boldsymbol{a}_N^{\text{H}}(\boldsymbol{p}, f_s)\, \boldsymbol{w}_s\right|^2\right) \tag{25a}$$

$$\text{subject to} \quad \pi_l \in \mathcal{T} \qquad \forall\, l \in \mathcal{L}. \tag{25b}$$

Due to the logarithm in (25a) and the unit-modulus constraints of analog beamforming vectors (i.e., $\left|[\boldsymbol{w}_s]_n\right| = 1, \forall n$), $\mathscr{P}_0$ is nonconvex. Moreover, due to the combinatorial nature of integer constraints (25b), $\mathscr{P}_0$ is NP-hard in which the optimal solution is intractable within polynomial time. To address these issues, we propose a novel beamforming optimization technique that consists of the following three major stages:

- *Quadratic transform:* We convert $\mathscr{P}_0$ to a quadratic optimization problem by isolating the quadratic array gains from its logarithm form.
- *Dynamic subarray connection via sparse recovery:* We map the TTD indices $\{\pi_l\}_{l=1}^L$ to the positions of non-zero elements of the sparse vectors $\{\tilde{\boldsymbol{e}}_l\}_{l=1}^L$.
- *Time delay/phase shift control via manifold optimization:* We optimize the time delays $\boldsymbol{\tau}$ and phase shifts $\boldsymbol{\theta}$ on the manifold of unit-modulus complex numbers.

B. Quadratic Transform

In this subsection, we convert the objective function (25a) to a sum-of-quadratics using the quadratic transform [41].

Proposition 1: By introducing auxiliary variables $\boldsymbol{\gamma} \triangleq [\gamma_1\ \gamma_2\ \cdots\ \gamma_S]^{\text{T}} \in \mathbb{R}^S$ and $\boldsymbol{\nu} \triangleq [\nu_1\ \nu_2\ \cdots\ \nu_S]^{\text{T}} \in \mathbb{C}^S$, $\mathscr{P}_0$ can be equivalently converted to $\mathscr{P}_1$ as

$$\mathscr{P}_1 : \quad \underset{\boldsymbol{\pi}, \boldsymbol{\tau}, \boldsymbol{\theta}, \boldsymbol{\gamma}, \boldsymbol{\nu}}{\text{maximize}} \quad f_1(\boldsymbol{\pi}, \boldsymbol{\tau}, \boldsymbol{\theta}, \boldsymbol{\gamma}, \boldsymbol{\nu}) \tag{26a}$$

$$\text{subject to} \quad \pi_l \in \mathcal{T} \qquad \forall\, l \in \mathcal{L} \tag{26b}$$

where f_1 is defined in (23) shown at the bottom of this page. □

Proof: See Appendix. ⊠

Since f_1 is a joint function of $(\boldsymbol{\pi}, \boldsymbol{\tau}, \boldsymbol{\theta}, \boldsymbol{\gamma}, \boldsymbol{\nu})$, it is challenging to determine them simultaneously. To address this issue, we use

$$f_1(\boldsymbol{\pi}, \boldsymbol{\tau}, \boldsymbol{\theta}, \boldsymbol{\gamma}, \boldsymbol{\nu}) \triangleq \sum_{s=1}^{S} \log_2(1 + \gamma_s) - \frac{1}{\ln 2} \sum_{s=1}^{S} \gamma_s - \frac{1}{\ln 2} \sum_{s=1}^{S} |\nu_s|^2 + \frac{2}{N \ln 2} \sum_{s=1}^{S} \sqrt{\rho_s(1 + \gamma_s)}\, \Re\{\nu_s^* \boldsymbol{a}_N^{\text{H}}(\boldsymbol{p}, f_s)\, \boldsymbol{w}_s\} - \frac{1}{N^2 \ln 2} \sum_{s=1}^{S} \rho_s |\nu_s|^2 \left|\boldsymbol{a}_N^{\text{H}}(\boldsymbol{p}, f_s)\, \boldsymbol{w}_s\right|^2. \tag{23}$$

an alternating approach that iteratively optimizes one variable while keeping the other variables fixed. For a given $(\boldsymbol{\pi}, \boldsymbol{\tau}, \boldsymbol{\theta}, \boldsymbol{\nu})$, the optimal solution $\boldsymbol{\gamma}^{\text{opt}} \triangleq [\,\gamma_1^{\text{opt}}\ \gamma_2^{\text{opt}}\ \cdots\ \gamma_S^{\text{opt}}\,]^{\text{T}}$ can be obtained by solving $\frac{\partial f_1}{\partial \boldsymbol{\gamma}} = \mathbf{0}_S$:

$$\gamma_s^{\text{opt}} = \frac{\rho_s}{N^2}\big|\boldsymbol{a}_N^{\text{H}}(\boldsymbol{p}, f_s)\,\boldsymbol{w}_s\big|^2 \qquad \forall\, s \in \mathcal{S}\,. \tag{27}$$

Also, for a given $(\boldsymbol{\pi}, \boldsymbol{\tau}, \boldsymbol{\theta}, \boldsymbol{\gamma})$, the optimal solution $\boldsymbol{\nu}^{\text{opt}} \triangleq [\,\nu_1^{\text{opt}}\ \nu_2^{\text{opt}}\ \cdots\ \nu_S^{\text{opt}}\,]^{\text{T}}$ can be obtained by solving $\frac{\partial f_1}{\partial \boldsymbol{\nu}} = \mathbf{0}_S$:

$$\nu_s^{\text{opt}} = \frac{N\sqrt{\rho_s(1+\gamma_s)}\,\boldsymbol{a}_N^{\text{H}}(\boldsymbol{p}, f_s)\,\boldsymbol{w}_s}{\rho_s\big|\boldsymbol{a}_N^{\text{H}}(\boldsymbol{p}, f_s)\,\boldsymbol{w}_s\big|^2 + N^2} \qquad \forall\, s \in \mathcal{S}\,. \tag{28}$$

Once we obtain $\boldsymbol{\gamma}^{\text{opt}}$ and $\boldsymbol{\nu}^{\text{opt}}$, we update $(\boldsymbol{\pi}, \boldsymbol{\tau}, \boldsymbol{\theta})$ by solving the reduced problem $\mathscr{P}_2$:

$$\mathscr{P}_2: \quad \underset{\boldsymbol{\pi}, \boldsymbol{\tau}, \boldsymbol{\theta}}{\text{maximize}} \quad f_2(\boldsymbol{\pi}, \boldsymbol{\tau}, \boldsymbol{\theta}) \tag{29a}$$

$$\text{subject to} \quad \pi_l \in \mathcal{T} \qquad \forall\, l \in \mathcal{L} \tag{29b}$$

where f_2 is defined as

$$f_2(\boldsymbol{\pi}, \boldsymbol{\tau}, \boldsymbol{\theta}) \triangleq \frac{2}{N}\sum_{s=1}^{S}\sqrt{\rho_s(1+\gamma_s)}\,\Re\{\nu_s^*\boldsymbol{a}_N^{\text{H}}(\boldsymbol{p}, f_s)\,\boldsymbol{w}_s\} - \frac{1}{N^2}\sum_{s=1}^{S}\rho_s|\nu_s|^2\big|\boldsymbol{a}_N^{\text{H}}(\boldsymbol{p}, f_s)\,\boldsymbol{w}_s\big|^2. \tag{30}$$

In the following subsections, we describe the alternating optimization operations that iteratively optimize $\boldsymbol{\pi}$ and $(\boldsymbol{\tau}, \boldsymbol{\theta})$.

C. Dynamic Subarray Connection Via Sparse Recovery

For a given $(\boldsymbol{\tau}, \boldsymbol{\theta}) = (\boldsymbol{\tau}^{\text{opt}}, \boldsymbol{\theta}^{\text{opt}})$, $\mathscr{P}_2$ is reduced to the subarray connection problem $\mathscr{P}_{2,\text{a}}$ as

$$\mathscr{P}_{2,\text{a}}: \quad \underset{\boldsymbol{\pi}}{\text{maximize}} \quad f_2\big(\boldsymbol{\pi}, \boldsymbol{\tau}^{\text{opt}}, \boldsymbol{\theta}^{\text{opt}}\big) \tag{31a}$$

$$\text{subject to} \quad \pi_l \in \mathcal{T} \qquad \forall\, l \in \mathcal{L}\,. \tag{31b}$$

Basically, $\mathscr{P}_{2,\text{a}}$ is a combinatorial optimization problem that requires an exhaustive search to determine the optimal solution. For example, if the number of TTDs is $T = 4$ and the number of PS subarrays is $L = 8$, then one needs to search all $T^L = 65,536$ combinations of $\boldsymbol{\pi}$ to obtain the optimal solution.

To find out a tractable solution of $\mathscr{P}_{2,\text{a}}$, we define a sparse subarray connection matrix $\tilde{\boldsymbol{E}} \triangleq [\,\tilde{\boldsymbol{e}}_1\ \tilde{\boldsymbol{e}}_2\ \cdots\ \tilde{\boldsymbol{e}}_L\,] \in \mathbb{R}^{T\times L}$ where $\tilde{\boldsymbol{e}}_l$ is a $T \times 1$ sparse vector defined as

$$[\tilde{\boldsymbol{e}}_l]_t = \begin{cases} 1 & \text{if } t = \pi_l \\ 0 & \text{otherwise}\,. \end{cases} \tag{32}$$

Then π_l is expressed as the nonzero element index of $\tilde{\boldsymbol{e}}_l$ as

$$\pi_l = \text{supp}\big(\tilde{\boldsymbol{e}}_l\big)\,. \tag{33}$$

Using $\tilde{\boldsymbol{E}}$, we can re-express $\boldsymbol{w}_s$ as a function of $\tilde{\boldsymbol{E}}$ as

$$\boldsymbol{w}_s = \boldsymbol{w}^{\text{ps}}\big(\boldsymbol{\theta}^{\text{opt}}\big) \odot \Big(\big(\tilde{\boldsymbol{E}}^{\text{T}}\boldsymbol{w}_s^{\text{ttd}}\big(\boldsymbol{\tau}^{\text{opt}}\big)\big) \otimes \mathbf{1}_K\Big) \tag{34}$$

$$= \text{diag}\big(\boldsymbol{w}^{\text{ps}}\big(\boldsymbol{\theta}^{\text{opt}}\big)\big)\big(\boldsymbol{I}_L \otimes \mathbf{1}_K\big)\tilde{\boldsymbol{E}}^{\text{T}}\boldsymbol{w}_s^{\text{ttd}}\big(\boldsymbol{\tau}^{\text{opt}}\big) \tag{35}$$

$$= \boldsymbol{A}\tilde{\boldsymbol{E}}^{\text{T}}\boldsymbol{b}_s \tag{36}$$

where $\boldsymbol{A} \in \mathbb{C}^{N\times L}$ and $\boldsymbol{b}_s \in \mathbb{C}^{T}$ are defined as

$$\boldsymbol{A} \triangleq \text{diag}\big(\boldsymbol{w}^{\text{ps}}\big(\boldsymbol{\theta}^{\text{opt}}\big)\big)\big(\boldsymbol{I}_L \otimes \mathbf{1}_K\big) \tag{37}$$

$$\boldsymbol{b}_s \triangleq \boldsymbol{w}_s^{\text{ttd}}\big(\boldsymbol{\tau}^{\text{opt}}\big)\,. \tag{38}$$

Then we recast the combinatorial optimization $\mathscr{P}_{2,\text{a}}$ to the sparse recovery problem $\mathscr{P}_{3,\text{a}}$ as

$$\mathscr{P}_{3,\text{a}}: \quad \underset{\tilde{\boldsymbol{E}}}{\text{maximize}} \quad f_3\big(\tilde{\boldsymbol{E}}\big) \tag{39a}$$

$$\text{subject to} \quad \|\tilde{\boldsymbol{e}}_l\|_0 \le 1 \qquad \forall\, l \in \mathcal{L} \tag{39b}$$

$$\mathbf{1}_T^{\text{T}}\tilde{\boldsymbol{e}}_l \le 1 \qquad \forall\, l \in \mathcal{L} \tag{39c}$$

where f_3 is defined as

$$f_3\big(\tilde{\boldsymbol{E}}\big) \triangleq \frac{2}{N}\sum_{s=1}^{S}\sqrt{\rho_s(1+\gamma_s)}\,\Re\{\nu_s^*\boldsymbol{a}_N^{\text{H}}(\boldsymbol{p}, f_s)\,\boldsymbol{A}\tilde{\boldsymbol{E}}^{\text{T}}\boldsymbol{b}_s\} - \frac{1}{N^2}\sum_{s=1}^{S}\rho_s|\nu_s|^2\big|\boldsymbol{a}_N^{\text{H}}(\boldsymbol{p}, f_s)\,\boldsymbol{A}\tilde{\boldsymbol{E}}^{\text{T}}\boldsymbol{b}_s\big|^2. \tag{40}$$

Although the integer constraints (31b) are replaced by the sparsity constraints (39b), $\mathscr{P}_{3,\text{a}}$ is still nonconvex due to the nonconvexity of ℓ_0-norm in (39b). To handle this issue, we use reweighted ℓ_2-norm approximation (RLA) that approximates the ℓ_0-norm as the weighted quadratic sum of elements [47], [48]. Specifically, $\|\tilde{\boldsymbol{e}}_l\|_0$ is approximated as

$$\|\tilde{\boldsymbol{e}}_l\|_0 \approx \sum_{t=1}^{T}p_{t,l}\big|[\tilde{\boldsymbol{e}}_l]_t\big|^2 = \|\boldsymbol{P}_l\tilde{\boldsymbol{e}}_l\|_2^2 \tag{41}$$

where $\boldsymbol{P}_l \triangleq \text{diag}(\sqrt{p_{1,l}}, \sqrt{p_{2,l}}, \cdots, \sqrt{p_{T,l}}) \in \mathbb{R}^{T\times T}$ and $p_{t,l} \ge 0$ is the RLA weight obtained from the subarray connection matrix $\tilde{\boldsymbol{E}}^{\text{prev}}$ of the previous iteration as

$$p_{t,l} \triangleq \Big(\big|[\tilde{\boldsymbol{e}}_l^{\text{prev}}]_t\big|^2 + \epsilon^{-1}\Big)^{-1}. \tag{42}$$

Here, $\epsilon > 0$ is used as an upper bound of $p_{l,t}$. By assigning larger RLA weights to the smaller elements and iteratively updating the RLA weights, RLA effectively penalizes these smaller elements, driving them closer to zero. In doing so, one can promote the sparsity of $\tilde{\boldsymbol{E}}$. By plugging (41) to (39b), we obtain the relaxed problem $\mathscr{P}_{4,\text{a}}$:

$$\mathscr{P}_{4,\text{a}}: \quad \underset{\tilde{\boldsymbol{E}}}{\text{maximize}} \quad f_3\big(\tilde{\boldsymbol{E}}\big) \tag{43a}$$

$$\text{subject to} \quad \|\boldsymbol{P}_l\tilde{\boldsymbol{e}}_l\|_2^2 \le 1 \qquad \forall\, l \in \mathcal{L} \tag{43b}$$

$$\mathbf{1}_T^{\text{T}}\tilde{\boldsymbol{e}}_l \le 1 \qquad \forall\, l \in \mathcal{L}\,. \tag{43c}$$

The relaxed problem $\mathscr{P}_{4,\text{a}}$ is a convex quadratic program that can be reformulated as a second-order cone program (SOCP). Using the convex optimization solver, we can obtain the global optimal solution $\tilde{\boldsymbol{E}}^{\text{opt}}$ of $\mathscr{P}_{4,\text{a}}$ [49]. We then set $\tilde{\boldsymbol{E}}^{\text{prev}} = \tilde{\boldsymbol{E}}^{\text{opt}}$ and update the RLA weight $p_{t,l}$ via (42). The RLA iteration is repeated until (39b) are satisfied. Once we have $\tilde{\boldsymbol{E}}^{\text{opt}}$, we obtain the TTD time delays $\boldsymbol{\pi}^{\text{opt}}$ via (33).

D. Time Delay/Phase Shift Control Via Manifold Optimization

For a given $\boldsymbol{\pi} = \boldsymbol{\pi}^{\mathrm{opt}}$, $\mathscr{P}_2$ is reduced to the time delay and phase shift control problem $\mathscr{P}_{2,\mathrm{b}}$ as

$$\mathscr{P}_{2,\mathrm{b}}: \quad \underset{\boldsymbol{\tau},\boldsymbol{\theta}}{\text{maximize}} \quad f_2\big(\boldsymbol{\pi}^{\mathrm{opt}}, \boldsymbol{\tau}, \boldsymbol{\theta}\big)\,. \tag{44}$$

Note that $\boldsymbol{w}_s$ is a function of the TTD beamforming vector $\boldsymbol{w}_s^{\mathrm{ttd}}(\boldsymbol{\tau})$ and the PS beamforming vector $\boldsymbol{w}^{\mathrm{ps}}(\boldsymbol{\theta})$ (see (21)). Since the elements of $\boldsymbol{w}_s^{\mathrm{ttd}}(\boldsymbol{\tau})$ and $\boldsymbol{w}^{\mathrm{ps}}(\boldsymbol{\theta})$ are unit-modulus, with phases controlled by $\boldsymbol{\tau}$ and $\boldsymbol{\theta}$ (see (8) and (9)), one cannot uniquely determine $\boldsymbol{\tau}$ and $\boldsymbol{\theta}$ due to the phase ambiguity issue. To address this issue, we redefine the optimization variables from $(\boldsymbol{\tau}, \boldsymbol{\theta})$ to $(\tilde{\boldsymbol{\tau}}, \tilde{\boldsymbol{\theta}}) \in \mathbb{C}^T \times \mathbb{C}^N$ as

$$\tilde{\boldsymbol{\tau}} \triangleq \big[\, e^{-jf_c\tau_1} \; e^{-jf_c\tau_2} \; \cdots \; e^{-jf_c\tau_T} \,\big]^{\mathrm{T}} \tag{45}$$

$$\tilde{\boldsymbol{\theta}} \triangleq \big[\, e^{-j\theta_1} \; e^{-j\theta_2} \; \cdots \; e^{-j\theta_N} \,\big]^{\mathrm{T}}. \tag{46}$$

Note that f_c is used in (45) to balance the magnitude difference between $\boldsymbol{\tau}$ and $\boldsymbol{\theta}$. Using $\tilde{\boldsymbol{\tau}}$ and $\tilde{\boldsymbol{\theta}}$, we can rewrite $\boldsymbol{w}_s$ as

$$\boldsymbol{w}_s = \tilde{\boldsymbol{\theta}} \odot \Big(\Big(\boldsymbol{E}_{\boldsymbol{\pi}^{\mathrm{opt}}}^{\mathrm{T}} \tilde{\boldsymbol{\tau}}^{\left(2\pi \frac{f_s}{f_c}\right)}\Big) \otimes \boldsymbol{1}_K\Big) \tag{47}$$

$$= \mathrm{diag}\big(\tilde{\boldsymbol{\theta}}\big)(\boldsymbol{I}_L \otimes \boldsymbol{1}_K)\, \boldsymbol{E}_{\boldsymbol{\pi}^{\mathrm{opt}}}^{\mathrm{T}} \tilde{\boldsymbol{\tau}}^{\left(2\pi \frac{f_s}{f_c}\right)} \tag{48}$$

$$= \mathrm{diag}\big(\tilde{\boldsymbol{\theta}}\big)\, \boldsymbol{C}\, \tilde{\boldsymbol{\tau}}^{\left(2\pi \frac{f_s}{f_c}\right)} \tag{49}$$

where $\boldsymbol{C} \in \mathbb{R}^{N\times T}$ is defined as

$$\boldsymbol{C} \triangleq (\boldsymbol{I}_L \otimes \boldsymbol{1}_K)\, \boldsymbol{E}_{\boldsymbol{\pi}^{\mathrm{opt}}}^{\mathrm{T}}\,. \tag{50}$$

Then $\mathscr{P}_{2,\mathrm{b}}$ can be reformulated as an optimization problem $\mathscr{P}_{3,\mathrm{b}}$ with unit-modulus constraints as

$$\mathscr{P}_{3,\mathrm{b}}: \quad \underset{\tilde{\boldsymbol{\tau}},\tilde{\boldsymbol{\theta}}}{\text{maximize}} \quad f_4\big(\tilde{\boldsymbol{\tau}}, \tilde{\boldsymbol{\theta}}\big) \tag{51a}$$

$$\text{subject to} \quad |[\,\tilde{\boldsymbol{\tau}}\,]_t| = 1 \qquad \forall t \in \mathcal{T} \tag{51b}$$

$$\big|\big[\,\tilde{\boldsymbol{\theta}}\,\big]_n\big| = 1 \qquad \forall n \in \mathcal{N} \tag{51c}$$

where f_4 is defined as

$$\begin{aligned} &f_4\big(\tilde{\boldsymbol{\tau}}, \tilde{\boldsymbol{\theta}}\big) \\ &\triangleq \frac{2}{N}\sum_{s=1}^{S}\sqrt{\rho_s(1+\gamma_s)}\,\Re\Big\{\nu_s^* \boldsymbol{a}_N^{\mathrm{H}}(\boldsymbol{p}, f_s)\,\mathrm{diag}\big(\tilde{\boldsymbol{\theta}}\big)\,\boldsymbol{C}\tilde{\boldsymbol{\tau}}^{\left(2\pi\frac{f_s}{f_c}\right)}\Big\} \\ &\quad - \frac{1}{N^2}\sum_{s=1}^{S}\rho_s|\nu_s|^2\Big|\boldsymbol{a}_N^{\mathrm{H}}(\boldsymbol{p}, f_s)\,\mathrm{diag}\big(\tilde{\boldsymbol{\theta}}\big)\,\boldsymbol{C}\tilde{\boldsymbol{\tau}}^{\left(2\pi\frac{f_s}{f_c}\right)}\Big|^2. \end{aligned} \tag{52}$$

Due to the nonconvexity of the unit-modulus constraints (51b) and (51c), $\mathscr{P}_{3,\mathrm{b}}$ is a nonconvex problem. To handle the unit-modulus constraints, we exploit the fact that the set of unit-modulus vectors form a Riemannian manifold, a generalization of the Euclidean space that enables the definition of differentiable structures on abstract and curved spaces [50]. Using the notion of Riemannian manifold, we can convert $\mathscr{P}_{3,\mathrm{b}}$ to an unconstrained optimization problem on the Riemannian manifold, where optimization techniques in the Euclidean space (e.g., conjugate gradient method) can be readily extended to determine the optimal $\tilde{\boldsymbol{\tau}}$ and $\tilde{\boldsymbol{\theta}}$ on the Riemannian manifold [51]. Put it formally, a Riemannian manifold $(\mathcal{M}, g)$ is a smooth manifold $\mathcal{M}$ equipped with a family g of smoothly-varying positive-definite inner products (i.e., Riemannian metric) on the tangent space $\mathcal{T}_p\,\mathcal{M}$ at each point $p \in \mathcal{M}$ [52]. A smooth manifold $\mathcal{M}$ is a topological space that locally resembles Euclidean space and is equipped with a smooth structure. Also, the tangent space $\mathcal{T}_p\,\mathcal{M} \triangleq \{\gamma'(0) : \gamma : \mathcal{I}(\subseteq \mathbb{R}) \to \mathcal{M},\, \gamma(0) = p\}$ at a point $p \in \mathcal{M}$ is a vector space containing tangent vectors at p. The Riemannian metric endows the smooth manifold with notions of length, angle, and distance between points on the manifold, from which the notion of gradient on the Riemannian manifold (i.e., Riemannian gradient) is defined.

Let $\mathcal{C}^1 \triangleq \{z \in \mathbb{C} \mid |z| = 1\}$ be the set of unit-modulus complex numbers. It has been shown that $\mathcal{C}^1$ is a submanifold of $\mathbb{C}$, meaning that $\mathcal{C}^1$ is a subset of $\mathbb{C}$ that is itself a smooth manifold. Also, since $\mathcal{C}^1$ is an embedded manifold of $\mathbb{C}$, it naturally inherits the Riemannian metric g_1 of $\mathbb{C}$ defined as $g_1(z_1, z_2) = \Re\{z_1^* z_2\}$ for all $z_1, z_2 \in \mathbb{C}$. Let us define the combined time delay and phase shift vector $\boldsymbol{\psi} \in \mathbb{C}^{T+N}$ as

$$\boldsymbol{\psi} \triangleq \big[\, \tilde{\boldsymbol{\tau}}^{\mathrm{T}} \; \tilde{\boldsymbol{\theta}}^{\mathrm{T}} \,\big]^{\mathrm{T}}. \tag{53}$$

The set of $\boldsymbol{\psi}$ is expressed as a Cartesian product of $\mathcal{C}^1$ as

$$\mathcal{C}^{T+N} \triangleq \big\{\boldsymbol{\psi} \in \mathbb{C}^{T+N} \,:\, |[\boldsymbol{\psi}]_i| = 1,\, \forall\, i\big\} = \prod_{i=1}^{T+N} \mathcal{C}^1. \tag{54}$$

Note that $\mathcal{C}^{T+N}$ is a product Riemannian manifold endowed with a Riemannian metric $g : \mathcal{T}_{\boldsymbol{\psi}}\,\mathcal{C}^{T+N} \times \mathcal{T}_{\boldsymbol{\psi}}\,\mathcal{C}^{T+N} \to \mathbb{R}$ defined as $g(\boldsymbol{p}, \boldsymbol{q}) = \Re\{\boldsymbol{p}^{\mathrm{H}}\boldsymbol{q}\}$ for all $\boldsymbol{p}, \boldsymbol{q} \in \mathcal{T}_{\boldsymbol{\psi}}\,\mathcal{C}^{T+N}$. Also, since the tangent space $\mathcal{T}_\psi\,\mathcal{C}^1$ of $\mathcal{C}^1$ at $\psi \in \mathcal{C}^1$ is $\mathcal{T}_\psi\,\mathcal{C}^1 = \{p \in \mathbb{C} : \Re\{p^*\psi\} = 0\}$, $\mathcal{T}_{\boldsymbol{\psi}}\,\mathcal{C}^{T+N}$ of $\mathcal{C}^{T+N}$ at $\boldsymbol{\psi} \in \mathcal{C}^{T+N}$ is[5]

$$\mathcal{T}_{\boldsymbol{\psi}}\,\mathcal{C}^{T+N} = \big\{\boldsymbol{p} \in \mathbb{C}^{T+N} \,:\, \Re\big\{[\boldsymbol{p}]_i^*[\boldsymbol{\psi}]_i\big\} = 0,\, \forall\, i\big\}\,. \tag{55}$$

Then $\mathscr{P}_{3,\mathrm{b}}$ can be reformulated as

$$\mathscr{P}_{3,\mathrm{b}}: \quad \underset{\boldsymbol{\psi}\in\mathcal{C}^{T+N}}{\text{maximize}} \quad f_4(\boldsymbol{\psi})\,. \tag{56}$$

Next, we explain the Riemannian conjugate gradient (RCG) method to determine $\boldsymbol{\psi} \in \mathcal{C}^{T+N}$ that maximizes $f_4(\boldsymbol{\psi})$. When compared to the traditional conjugate gradient method, it requires two additional operations to determine the optimal solution on the manifold: 1) the *projection* that projects the search direction onto the tangent space; and 2) the *retraction* that maps the updated point back to the manifold [51].

First, the orthogonal projection of $\boldsymbol{p} \in \mathbb{C}^{T+N}$ onto the tangent space $\mathcal{T}_{\boldsymbol{\psi}}\,\mathcal{C}^{T+N}$ is a unique vector $\mathrm{proj}_{\mathcal{T}_{\boldsymbol{\psi}}\,\mathcal{C}^{T+N}}(\boldsymbol{p})$ that satisfies $g(\boldsymbol{p} - \mathrm{proj}_{\mathcal{T}_{\boldsymbol{\psi}}\mathcal{C}^{T+N}}(\boldsymbol{p}), \boldsymbol{q}) = 0$ for all $\boldsymbol{q} \in \mathcal{T}_{\boldsymbol{\psi}}\,\mathcal{C}^{T+N}$.

Lemma 1: The orthogonal projection $\mathrm{proj}_{\mathcal{T}_{\boldsymbol{\psi}}\,\mathcal{C}^{T+N}} : \mathbb{C}^{T+N} \to \mathcal{T}_{\boldsymbol{\psi}}\,\mathcal{C}^{T+N}$ onto the tangent space $\mathcal{T}_{\boldsymbol{\psi}}\,\mathcal{C}^{T+N}$ at $\boldsymbol{\psi} \in \mathcal{C}^{T+N}$ is defined as [53]

$$\mathrm{proj}_{\mathcal{T}_{\boldsymbol{\psi}}\,\mathcal{C}^{T+N}}(\boldsymbol{p}) = \boldsymbol{p} - \Re\big\{\boldsymbol{p}^* \odot \boldsymbol{\psi}\big\} \odot \boldsymbol{\psi} \tag{57}$$

for all $\boldsymbol{p} \in \mathbb{C}^{T+N}$. □

Using the projection operator, we can obtain the Riemannian gradient, which indicates the steepest descent direction of f_4 in the tangent space. In fact, since $\mathcal{C}^{T+N}$ is an embedded manifold of $\mathbb{C}^{T+N}$, the Riemannian gradient can be obtained by projecting the Euclidean gradient onto the tangent space.

[5]The Riemannian metric g of the product space $\mathcal{M} = \mathcal{M}_1 \times \mathcal{M}_2$ of Riemannian manifolds $(\mathcal{M}_1, g_1)$ and $(\mathcal{M}_2, g_2)$ is $g((v_1, v_2), (w_1, w_2)) = g_1(v_1, w_1) + g_2(v_2, w_2)$ for all $v_1, w_1 \in \mathcal{M}_1$ and $v_2, w_2 \in \mathcal{M}_2$. Also, the tangent space of $\mathcal{M}$ at (v_1, v_2) is $\mathcal{T}_{(v_1,v_2)}\,\mathcal{M} = \mathcal{T}_{v_1}\,\mathcal{M}_1 \times \mathcal{T}_{v_2}\,\mathcal{M}_2$.

Lemma 2: The Riemannian gradient $\mathrm{grad}\, f_4(\boldsymbol{\psi})$ of f_4 at $\boldsymbol{\psi} \in \mathcal{C}^{T+N}$ can be obtained by projecting the complex Euclidean gradient $\nabla_{\boldsymbol{\psi}} f_4(\boldsymbol{\psi})$ onto the tangent space $\mathcal{T}_{\boldsymbol{\psi}}\, \mathcal{C}^{T+N}$ as [53]

$$\mathrm{grad}\, f_4(\boldsymbol{\psi}) = \mathrm{proj}_{\mathcal{T}_{\boldsymbol{\psi}}\, \mathcal{C}^{T+N}}\big(\nabla_{\boldsymbol{\psi}} f_4(\boldsymbol{\psi})\big) \tag{58}$$

$$= \nabla_{\boldsymbol{\psi}} f_4(\boldsymbol{\psi}) - \Re\big\{\nabla_{\boldsymbol{\psi}} f_4^*(\boldsymbol{\psi}) \odot \boldsymbol{\psi}\big\} \odot \boldsymbol{\psi} \tag{59}$$

where $\nabla_{\boldsymbol{\psi}} f_4(\boldsymbol{\psi}) = \big[\, \nabla_{\tilde{\boldsymbol{\tau}}} f_4^{\mathrm{T}}(\boldsymbol{\psi})\ \nabla_{\tilde{\boldsymbol{\theta}}} f_4^{\mathrm{T}}(\boldsymbol{\psi}) \,\big]^{\mathrm{T}} \in \mathbb{C}^{T+N}$ is in (61) and (62) shown at the bottom of the page. □

Proof: $\nabla_{\boldsymbol{\psi}} f_4(\boldsymbol{\psi})$ can be easily obtained by computing the derivative of f_4 with respect to $\tilde{\boldsymbol{\tau}}^*$ and $\tilde{\boldsymbol{\theta}}^*$. ⊠

Second, the retraction $\mathrm{retr}_{\boldsymbol{\psi}}$ is a mapping that projects the tangent vector onto $\mathcal{C}^{T+N}$ while preserving the local structure and directionality of $\boldsymbol{v}$. Put it formally, $\mathrm{retr}_{\boldsymbol{\psi}} : \mathcal{T}_{\boldsymbol{\psi}}\, \mathcal{C}^{T+N} \to \mathcal{C}^{T+N}$ is a smooth map that satisfies $\mathrm{retr}_{\boldsymbol{\psi}}(\mathbf{0}_{T+N}) = \boldsymbol{\psi}$ and $\frac{d}{dt}\mathrm{retr}_{\boldsymbol{\psi}}(t\boldsymbol{v})\big|_{t=0} = \boldsymbol{v}$ for all $\boldsymbol{v} \in \mathcal{T}_{\boldsymbol{\psi}}\, \mathcal{C}^{T+N}$.

Lemma 3: The retraction $\mathrm{retr}_{\boldsymbol{\psi}} : \mathcal{T}_{\boldsymbol{\psi}}\, \mathcal{C}^{T+N} \to \mathcal{C}^{T+N}$ onto $\mathcal{C}^{T+N}$ at $\boldsymbol{\psi} \in \mathcal{C}^{T+N}$ is defined as [53]

$$\mathrm{retr}_{\boldsymbol{\psi}}(\boldsymbol{v}) = \left[\, \frac{[\boldsymbol{\psi}+\boldsymbol{v}]_1}{|[\boldsymbol{\psi}+\boldsymbol{v}]_1|}\ \frac{[\boldsymbol{\psi}+\boldsymbol{v}]_2}{|[\boldsymbol{\psi}+\boldsymbol{v}]_2|} \cdots \frac{[\boldsymbol{\psi}+\boldsymbol{v}]_{T+N}}{|[\boldsymbol{\psi}+\boldsymbol{v}]_{T+N}|} \,\right]^{\mathrm{T}}. \tag{60}$$

for all $\boldsymbol{v} \in \mathcal{T}_{\boldsymbol{\psi}}\, \mathcal{C}$. □

The update equations for the conjugate direction $\boldsymbol{d}_i \in \mathcal{C}^{T+N}$ and $\boldsymbol{\psi}_i$ at the ith iteration are given by

$$\boldsymbol{d}_i = \mathrm{grad}\, f_4(\boldsymbol{\psi}_i) + \beta_i\, \mathrm{proj}_{\mathcal{T}_{\boldsymbol{\psi}_i}\, \mathcal{C}^{T+N}}(\boldsymbol{d}_{i-1}) \tag{63}$$

$$\boldsymbol{\psi}_{i+1} = \mathrm{retr}_{\boldsymbol{\psi}_i}(\alpha_i \boldsymbol{d}_i) \tag{64}$$

where α_i is the step size determined by the line search method and $\beta_i = \frac{\|\mathrm{grad}\, f_4(\boldsymbol{\psi}_i)\|_2^2}{\|\mathrm{grad}\, f_4(\boldsymbol{\psi}_{i-1})\|_2^2}$ is the Fletcher-Reeves conjugate gradient parameter [54], [55]. Note that in (63), the projection operator is used since $\mathrm{grad}\, f_4(\boldsymbol{\psi}_i) \in \mathcal{T}_{\boldsymbol{\psi}_i}\, \mathcal{C}^{T+N}$ whereas $\boldsymbol{d}_{i-1} \in \mathcal{T}_{\boldsymbol{\psi}_{i-1}}\, \mathcal{C}^{T+N}$. Also, in (64), the retraction operator is used to ensure $\boldsymbol{\psi}_i \in \mathcal{C}^{T+N}$. The update equations are repeated until $\boldsymbol{\psi}_i$ converges. Once we have the converged solution $\boldsymbol{\psi}^{\mathrm{opt}}$, we decompose $\boldsymbol{\psi}^{\mathrm{opt}}$ into $\tilde{\boldsymbol{\tau}}^{\mathrm{opt}}$ and $\tilde{\boldsymbol{\theta}}^{\mathrm{opt}}$ using (53), from which we obtain $\tau_t^{\mathrm{opt}} = -\frac{1}{f_{\mathrm{c}}}\angle\tilde{\tau}_t^{\mathrm{opt}}$ and $\theta_n^{\mathrm{opt}} = -\angle\tilde{\theta}_n^{\mathrm{opt}}$.

The dynamic subarray connection and time delay/phase shift control operations are repeated until $(\boldsymbol{\pi}, \boldsymbol{\tau}, \boldsymbol{\theta})$ converges. After obtaining the optimal solution $(\boldsymbol{\pi}^{\mathrm{opt}}, \boldsymbol{\tau}^{\mathrm{opt}}, \boldsymbol{\theta}^{\mathrm{opt}})$ of $\mathscr{P}_2$, we update the auxiliary variables $\boldsymbol{\gamma}$ and $\boldsymbol{\nu}$ using (27) and (28) and then repeat solving $\mathscr{P}_2$ until $(\boldsymbol{\pi}, \boldsymbol{\tau}, \boldsymbol{\theta})$ converges. Algorithm 1 summarizes the centralized dynamic subarray connection and time delay/phase shift control algorithm.

Algorithm 1: Centralized Dynamic Subarray Connection and Time Delay/Phase Shift Control Algorithm.

Input: Target direction $\boldsymbol{p}$, subcarrier channel SNR $\{\rho_s\}_{s=1}^S$, the numbers of TTDs and PS subarrays T and L
Initialize: $\boldsymbol{\pi} = [\,1\ 2 \cdots T\,]^{\mathrm{T}} \otimes \mathbf{1}_{L/T}$
  Set $\boldsymbol{\tau}$ and $\boldsymbol{\theta}$ as (12) and (13), respectively
while $(\boldsymbol{\pi}, \boldsymbol{\tau}, \boldsymbol{\theta}, \boldsymbol{\gamma}, \boldsymbol{\nu})$ do not converge **do**
  Update $\boldsymbol{\gamma}$ and $\boldsymbol{\nu}$ using (27) and (28)
  while $(\boldsymbol{\pi}, \boldsymbol{\tau}, \boldsymbol{\theta})$ do not converge **do**
    $\tilde{\boldsymbol{E}}$ = Reweighted ℓ_2-norm approximation $(\mathscr{P}_{3,\mathrm{a}})$
    $\pi_l = \mathrm{supp}(\tilde{\boldsymbol{e}}_l)$ $\quad \forall\, l \in \mathcal{L}$
    $\boldsymbol{\psi}$ = Riemannian conjugate gradient $(\mathcal{C}^{T+N}, \mathscr{P}_{3,\mathrm{b}})$
    $\big[\, \tilde{\boldsymbol{\tau}}^{\mathrm{T}}\ \tilde{\boldsymbol{\theta}}^{\mathrm{T}} \,\big]^{\mathrm{T}} = \boldsymbol{\psi}$
    $\tau_t = -\frac{1}{f_{\mathrm{c}}}\angle\tilde{\tau}_t,\ \theta_n = -\angle\tilde{\theta}_n$ $\quad \forall\, t \in \mathcal{T},\ n \in \mathcal{N}$
  end while
end while
Output: $\boldsymbol{\pi}, \boldsymbol{\tau}, \boldsymbol{\theta}$

Function Reweighted ℓ_2-norm approximation $(\mathscr{P})$
Solve $\mathscr{P}$ while ignoring the sparsity constraint
while the sparsity constraint is not satisfied **do**
  $\tilde{\boldsymbol{E}}^{\mathrm{prev}} = \tilde{\boldsymbol{E}}$
  $p_{t,l} = (|[\tilde{\boldsymbol{e}}_l^{\mathrm{prev}}]_t|^2 + \epsilon^{-1})^{-1}$ $\quad \forall\, t \in \mathcal{T},\ n \in \mathcal{N}$
  $\|\tilde{\boldsymbol{e}}_l\|_0 \approx \big\|\mathrm{diag}(\sqrt{p_{l,1}}, \sqrt{p_{l,2}}, \cdots, \sqrt{p_{l,T}})\tilde{\boldsymbol{e}}\big\|_2^2$ $\quad \forall\, l \in \mathcal{L}$
  Solve the relaxed problem via SOCP solver
end while
Output: $\tilde{\boldsymbol{E}}$

Function Riemannian conjugate gradient $(\mathcal{C}, \mathscr{P})$
$\boldsymbol{\psi}_0 = \mathbf{1}$, $\boldsymbol{d}_0 = \mathbf{0}$, $i = 1$
while $\boldsymbol{\psi}_i$ do not converge **do**
  $\mathrm{grad}\, f(\boldsymbol{\psi}_i) = \mathrm{proj}_{\mathcal{T}_{\boldsymbol{\psi}_i}\, \mathcal{C}}(\nabla_{\boldsymbol{\psi}} f(\boldsymbol{\psi}_i))$
  $\beta_i = \frac{\|\mathrm{grad}\, f(\boldsymbol{\psi}_i)\|_2^2}{\|\mathrm{grad}\, f(\boldsymbol{\psi}_{i-1})\|_2^2}$
  $\boldsymbol{d}_i = \mathrm{grad}\, f(\boldsymbol{\psi}_i) + \beta_i\, \mathrm{proj}_{\mathcal{T}_{\boldsymbol{\psi}_i}\, \mathcal{C}}(\boldsymbol{d}_{i-1})$
  Find a step size $\alpha_i > 0$ via line search
  $\boldsymbol{\psi}_{i+1} = \mathrm{retr}_{\boldsymbol{\psi}_i}(\alpha_i \boldsymbol{d}_i)$
  $i = i + 1$
end while
Output: $\boldsymbol{\psi}$

IV. Wideband Dynamic Array-of-Subarray Architecture: Distributed Approach

While the beamforming optimization algorithm in Section III is effective at maximizing the total array gain, it might be

$$\nabla_{\tilde{\boldsymbol{\tau}}} f_4(\boldsymbol{\psi}) = \frac{2\pi}{N}\sum_{s=1}^{S}\frac{f_s}{f_{\mathrm{c}}}\left(\nu_s\sqrt{\rho_s(1+\gamma_s)} - \frac{\rho_s|\nu_s|^2}{N}\boldsymbol{a}_N^{\mathrm{H}}(\boldsymbol{p}, f_s)\mathrm{diag}\big(\tilde{\boldsymbol{\theta}}\big)\boldsymbol{C}\tilde{\boldsymbol{\tau}}^{\left(2\pi\frac{f_s}{f_{\mathrm{c}}}\right)}\right)\mathrm{diag}\Big(\tilde{\boldsymbol{\tau}}^{\left(1-2\pi\frac{f_s}{f_{\mathrm{c}}}\right)}\Big)\boldsymbol{C}^{\mathrm{H}}\big(\mathrm{diag}\big(\tilde{\boldsymbol{\theta}}\big)\big)^{\mathrm{H}}\boldsymbol{a}_N(\boldsymbol{p}, f_s) \tag{61}$$

$$\nabla_{\tilde{\boldsymbol{\theta}}} f_4(\boldsymbol{\psi}) = \frac{1}{N}\sum_{s=1}^{S}\left(\nu_s\sqrt{\rho_s(1+\gamma_s)} - \frac{\rho_s|\nu_s|^2}{N}\Big(\tilde{\boldsymbol{\tau}}^{\left(2\pi\frac{f_s}{f_{\mathrm{c}}}\right)}\Big)^{\mathrm{T}}\boldsymbol{C}^{\mathrm{T}}\big(\mathrm{diag}\big(\boldsymbol{a}_N(\boldsymbol{p}, f_s)\big)\big)^{\mathrm{H}}\tilde{\boldsymbol{\theta}}\right)\mathrm{diag}\big(\boldsymbol{a}_N(\boldsymbol{p}, f_s)\big)\boldsymbol{C}^*(\tilde{\boldsymbol{\tau}}^*)^{\left(2\pi\frac{f_s}{f_{\mathrm{c}}}\right)} \tag{62}$$

computationally burdensome when the number of antennas N is extremely large since its computational complexity is proportional to N. We note that among the three variables, i.e., subarray connection vector $\boldsymbol{\pi} \in \mathbb{N}^L$, time delay vector $\boldsymbol{\tau} \in \mathbb{R}^T$, and PS phase shift vector $\boldsymbol{\theta} \in \mathbb{R}^N$, $\boldsymbol{\theta}$ has the greatest impact on the computational complexity. Thus, we present a distributed beamforming optimization framework that optimizes $\boldsymbol{\pi}$ and $\boldsymbol{\tau}$ in a centralized manner while $\boldsymbol{\theta}$ is optimized in a distributed manner at the subarray level.

A. Array Gain Decomposition

In this subsection, we will show that the array gain $G(\boldsymbol{w}_s, \boldsymbol{p})$ can be expressed as a sum of subarray gains $\{G_t(\boldsymbol{w}_{s,t}, \boldsymbol{p})\}_{t=1}^T$ where the magnitudes are determined by the phase shifts of the PS subarray and the arguments are determined by the TTD time delay. These observations lay the foundation for the development of our distributed optimization framework. Let $\mathcal{N}_t \subseteq \mathcal{N}$ be the set of antenna element indices connected to the tth TTD as

$$\mathcal{N}_t \triangleq \{(l-1)K + k \in \mathcal{N} \,:\, \pi_l = t, k = 1, 2, \ldots, K\}. \quad (65)$$

Also, let $\boldsymbol{a}_{N,t}(\boldsymbol{p}, f_s) \in \mathbb{C}^{|\mathcal{N}_t|}$ and $\boldsymbol{w}_{s,t} \in \mathbb{C}^{|\mathcal{N}_t|}$ be the corresponding subvectors of $\boldsymbol{a}_N(\boldsymbol{p}, f_s)$ and $\boldsymbol{w}_s$, respectively:

$$\boldsymbol{a}_{N,t}(\boldsymbol{p}, f_s) \triangleq \big[[\boldsymbol{a}_N(\boldsymbol{p}, f_s)]_n \,:\, n \in \mathcal{N}_t\big]^{\mathrm{T}} \quad (66)$$

$$\boldsymbol{w}_{s,t} \triangleq \big[[\boldsymbol{w}_s]_n \,:\, n \in \mathcal{N}_t\big]^{\mathrm{T}} \quad (67)$$

$$= e^{-j2\pi f_s \tau_t} \boldsymbol{w}^{\mathrm{ps}}(\boldsymbol{\theta}_{\mathcal{N}_t}) \quad (68)$$

where $\boldsymbol{\theta}_{\mathcal{N}_t} \in \mathbb{R}^{|\mathcal{N}_t|}$ is the corresponding subvector of $\boldsymbol{\theta}$:

$$\boldsymbol{\theta}_{\mathcal{N}_t} \triangleq [\,\theta_n \,:\, n \in \mathcal{N}_t]^{\mathrm{T}}. \quad (69)$$

The tth subarray gain $G_t(\boldsymbol{w}_{s,t}, \boldsymbol{p})$ of $\boldsymbol{w}_{s,t}$ at the target direction $\boldsymbol{p}$ is defined as

$$G_t(\boldsymbol{w}_{s,t}, \boldsymbol{p}) \triangleq \boldsymbol{a}_{N,t}^{\mathrm{H}}(\boldsymbol{p}, f_s)\, \boldsymbol{w}_{s,t} \quad (70)$$

$$= e^{-j2\pi f_s \tau_t} \boldsymbol{a}_{N,t}^{\mathrm{H}}(\boldsymbol{p}, f_s)\, \boldsymbol{w}^{\mathrm{ps}}(\boldsymbol{\theta}_{\mathcal{N}_t}). \quad (71)$$

Then $G(\boldsymbol{w}_s, \boldsymbol{p})$ is expressed as a sum of $\{G_t(\boldsymbol{w}_{s,t}, \boldsymbol{p})\}_{t=1}^T$ as

$$G(\boldsymbol{w}_s, \boldsymbol{p}) = \sum_{t=1}^{T} \boldsymbol{a}_{N,t}^{\mathrm{H}}(\boldsymbol{p}, f_s)\, \boldsymbol{w}_{s,t} \quad (72)$$

$$= \sum_{t=1}^{T} G_t(\boldsymbol{w}_{s,t}, \boldsymbol{p}). \quad (73)$$

Remark 1: Let $m_{s,t}$ and $v_{s,t}$ be the magnitude and argument of the tth subarray gain $G_t(\boldsymbol{w}_{s,t}, \boldsymbol{p})$. Then $m_{s,t}$ is a sole function of $\boldsymbol{\theta}_{\mathcal{N}_t}$, whereas $v_{s,t}$ is determined by τ_t and $\boldsymbol{\theta}_{\mathcal{N}_t}$:

$$m_{s,t} \triangleq |G_t(\boldsymbol{w}_{s,t}, \boldsymbol{p})| \quad (74)$$

$$= \big|\boldsymbol{a}_{N,t}^{\mathrm{H}}(\boldsymbol{p}, f_s)\, \boldsymbol{w}^{\mathrm{ps}}(\boldsymbol{\theta}_{\mathcal{N}_t})\big| \quad (75)$$

$$v_{s,t} \triangleq \angle G_t(\boldsymbol{w}_{s,t}, \boldsymbol{p}) \quad (76)$$

$$= -2\pi f_s \tau_t + \angle\big(\boldsymbol{a}_{N,t}^{\mathrm{H}}(\boldsymbol{p}, f_s)\, \boldsymbol{w}^{\mathrm{ps}}(\boldsymbol{\theta}_{\mathcal{N}_t})\big). \quad (77)$$

□

Remark 2: The absolute square of the array gain $G(\boldsymbol{w}_s, \boldsymbol{p})$ is expressed as a function of $\{m_{s,t}\}_{s,t}$ and $\{v_{s,t}\}_{s,t}$ as

$$|G(\boldsymbol{w}_s, \boldsymbol{p})|^2 = \left|\sum_{t=1}^{T} G_t(\boldsymbol{w}_{s,t}, \boldsymbol{p})\right|^2 = \left|\sum_{t=1}^{T} m_{s,t} e^{j v_{s,t}}\right|^2. \quad (78)$$

□

Remarks 1 and 2 imply that the array gain maximization problem can be decoupled into the subarray gain maximization problems by treating $\{m_{s,t}\}_{s,t}$ and $\{v_{s,t}\}_{s,t}$ as independent variables. Based on this, we formulate the beamforming optimization problem $\tilde{\mathscr{P}}_0$ to determine $\boldsymbol{\pi}$, $\boldsymbol{\tau}$, and $\{\boldsymbol{\theta}_{\mathcal{N}_t}\}_{t=1}^T$ maximizing the sum of squares of array gains as

$$\tilde{\mathscr{P}}_0 : \quad \underset{\boldsymbol{\pi}, \boldsymbol{\tau}, \{\boldsymbol{\theta}_{\mathcal{N}_t}\}_{t=1}^T}{\text{maximize}} \quad \sum_{s=1}^{S} |G(\boldsymbol{w}_s, \boldsymbol{p})|^2 \quad (79a)$$

$$\text{subject to} \quad \pi_l \in \mathcal{T} \quad \forall\, l \in \mathcal{L}. \quad (79b)$$

To solve $\tilde{\mathscr{P}}_0$, we use the alternating approach that first fixes $\{\boldsymbol{\theta}_{\mathcal{N}_t}\}_{t=1}^T$ and optimizes $(\boldsymbol{\pi}, \boldsymbol{\tau})$ in a centralized manner. We then fix $(\boldsymbol{\pi}, \boldsymbol{\tau})$ and optimize $\{\boldsymbol{\theta}_{\mathcal{N}_t}\}_{t=1}^T$ in a distributed manner.

B. Centralized Subarray Connection and Time Delay Control

For a given $(\boldsymbol{\tau}, \{\boldsymbol{\theta}_{\mathcal{N}_t}\}_{t=1}^T) = (\boldsymbol{\tau}^{\mathrm{opt}}, \{\boldsymbol{\theta}_{\mathcal{N}_t}^{\mathrm{opt}}\}_{t=1}^T)$, $\tilde{\mathscr{P}}_0$ is reduced to the subarray connection problem $\tilde{\mathscr{P}}_{0,\mathrm{a}}$ as

$$\tilde{\mathscr{P}}_{0,\mathrm{a}} : \quad \underset{\boldsymbol{\pi}}{\text{maximize}} \quad \sum_{s=1}^{S} \big|\boldsymbol{a}_N^{\mathrm{H}}(\boldsymbol{p}, f_s)\, \boldsymbol{w}_s\big|^2 [-6pt] \quad (80a)$$

$$\text{subject to} \quad \pi_l \in \mathcal{T} \quad \forall\, l \in \mathcal{L}. \quad (80b)$$

Similar to the dynamic subarray connection operation in Section III-C, we change the optimization variable from the subarray connection vector $\boldsymbol{\pi}$ to the sparse subarray connection matrix $\tilde{\boldsymbol{E}} = [\,\tilde{e}_1\, \tilde{e}_2 \cdots \tilde{e}_L]$ (see (32)) to obtain the modified sparse recovery problem $\tilde{\mathscr{P}}_{1,\mathrm{a}}$ as

$$\tilde{\mathscr{P}}_{1,\mathrm{a}} : \quad \underset{\tilde{\boldsymbol{E}}}{\text{maximize}} \quad \sum_{s=1}^{S} \big|\boldsymbol{a}_N^{\mathrm{H}}(\boldsymbol{p}, f_s)\, \boldsymbol{A}\tilde{\boldsymbol{E}}^{\mathrm{T}} \boldsymbol{b}_s\big|^2 \quad (81a)$$

$$\text{subject to} \quad \|\tilde{e}_l\|_0 \le 1 \quad \forall\, l \in \mathcal{L} \quad (81b)$$

$$\boldsymbol{1}_T^{\mathrm{T}} \tilde{e}_l \le 1 \quad \forall\, l \in \mathcal{L} \quad (81c)$$

where $\boldsymbol{A}$ and $\boldsymbol{b}_s$ are defined in (37) and (38).

Note that $\tilde{\mathscr{P}}_{1,\mathrm{a}}$ is a maximization problem with a quadratic objective function. To deal with this issue, we use successive convex approximation (SCA) which approximates the quadratic objective function (81a) to a linear function by using the first-order Taylor expansion. We first rewrite the objective function (81a) of $\tilde{\mathscr{P}}_{1,\mathrm{a}}$ as

$$f_4(\tilde{\boldsymbol{E}}) \triangleq \sum_{s=1}^{S} \big|\boldsymbol{a}_N^{\mathrm{H}}(\boldsymbol{p}, f_s)\, \boldsymbol{A}\tilde{\boldsymbol{E}}^{\mathrm{T}} \boldsymbol{b}_s\big|^2 \quad (82)$$

$$= \big\|\boldsymbol{D}^{\mathrm{T}} \mathrm{vec}(\tilde{\boldsymbol{E}})\big\|_2^2 \quad (83)$$

where $\boldsymbol{D} \triangleq [\boldsymbol{D}_1 \ \boldsymbol{D}_2 \cdots \boldsymbol{D}_S] \in \mathbb{R}^{TL\times 2S}$ and $\boldsymbol{D}_s \in \mathbb{R}^{TL\times 2}$ is defined as

$$\boldsymbol{D}_s \triangleq \left[\Re\left\{\left(\boldsymbol{A}^{\mathrm{T}}\boldsymbol{a}_N^*(\boldsymbol{p}, f_s)\right)\otimes \boldsymbol{b}_s\right\} \ \Im\left\{\left(\boldsymbol{A}^{\mathrm{T}}\boldsymbol{a}_N^*(\boldsymbol{p}, f_s)\right)\otimes \boldsymbol{b}_s\right\}\right]. \tag{84}$$

Then, for a given $\tilde{\boldsymbol{E}}^{\mathrm{prev}}$ obtained at the previous SCA iteration, the first-order Taylor expansion $F(\tilde{\boldsymbol{E}} \mid \tilde{\boldsymbol{E}}^{\mathrm{prev}})$ of $f_4(\tilde{\boldsymbol{E}})$ is

$$F\left(\tilde{\boldsymbol{E}} \mid \tilde{\boldsymbol{E}}^{\mathrm{prev}}\right)$$
$$\triangleq f_4\left(\tilde{\boldsymbol{E}}\right) + \nabla_{\mathrm{vec}(\tilde{\boldsymbol{E}})} f_4\left(\tilde{\boldsymbol{E}}^{\mathrm{prev}}\right)^{\mathrm{T}} \mathrm{vec}\left(\tilde{\boldsymbol{E}} - \tilde{\boldsymbol{E}}^{\mathrm{prev}}\right) \tag{85}$$
$$= \mathrm{vec}\left(\tilde{\boldsymbol{E}}^{\mathrm{prev}}\right)^{\mathrm{T}} \boldsymbol{D}\boldsymbol{D}^{\mathrm{T}} \mathrm{vec}\left(2\tilde{\boldsymbol{E}} - \tilde{\boldsymbol{E}}^{\mathrm{prev}}\right) \tag{86}$$
$$= 2\sum_{l=1}^{L} \boldsymbol{d}_l^{\mathrm{T}} \tilde{\boldsymbol{e}}_l - \left\|\boldsymbol{D}^{\mathrm{T}} \mathrm{vec}\left(\tilde{\boldsymbol{E}}^{\mathrm{prev}}\right)\right\|_2^2 \tag{87}$$

where $\boldsymbol{d}_l \in \mathbb{R}^T$ is the lth subvector of $\boldsymbol{D}\boldsymbol{D}^{\mathrm{T}}\mathrm{vec}(\tilde{\boldsymbol{E}}^{\mathrm{prev}}) \in \mathbb{R}^{TL}$ such that

$$\boldsymbol{D}\boldsymbol{D}^{\mathrm{T}}\mathrm{vec}\left(\tilde{\boldsymbol{E}}^{\mathrm{prev}}\right) = \left[\, \boldsymbol{d}_1^{\mathrm{T}} \ \boldsymbol{d}_2^{\mathrm{T}} \ \cdots \ \boldsymbol{d}_L^{\mathrm{T}} \,\right]^{\mathrm{T}}. \tag{88}$$

By substituting $f_4(\tilde{\boldsymbol{E}})$ with $F(\tilde{\boldsymbol{E}} \mid \tilde{\boldsymbol{E}}^{\mathrm{prev}})$, we obtain the relaxed SCA problem $\tilde{\mathscr{P}}_{2,\mathrm{a}}$ as

$$\tilde{\mathscr{P}}_{2,\mathrm{a}}: \quad \underset{\tilde{\boldsymbol{E}}}{\text{maximize}} \quad \sum_{l=1}^{L} \boldsymbol{d}_l^{\mathrm{T}} \tilde{\boldsymbol{e}}_l \tag{89a}$$
$$\text{subject to} \quad \|\tilde{\boldsymbol{e}}_l\|_0 \le 1 \qquad \forall\, l \in \mathcal{L} \tag{89b}$$
$$\boldsymbol{1}_T^{\mathrm{T}} \tilde{\boldsymbol{e}}_l \le 1 \qquad \forall\, l \in \mathcal{L}\,. \tag{89c}$$

Since $f_4(\tilde{\boldsymbol{E}})$ is convex, $F(\tilde{\boldsymbol{E}} \mid \tilde{\boldsymbol{E}}^{\mathrm{prev}}) \le f_4(\tilde{\boldsymbol{E}})$ and thus, the optimal value of $\tilde{\mathscr{P}}_{2,\mathrm{a}}$ is a lower bound of that of $\tilde{\mathscr{P}}_{1,\mathrm{a}}$. One can easily see that the optimal solution $\{\tilde{\boldsymbol{e}}_l^{\mathrm{opt}}\}_{l=1}^{L}$ of $\tilde{\mathscr{P}}_{2,\mathrm{a}}$ is

$$\tilde{\boldsymbol{e}}_l^{\mathrm{opt}} = \begin{cases} \boldsymbol{e}_{t_{\max}} & \text{if } [\boldsymbol{d}_l]_{t_{\max}} > 0 \\ \boldsymbol{0}_T & \text{otherwise} \end{cases} \tag{90}$$

where $t_{\max}$ is the maximum element index of $\boldsymbol{d}_l$ given by

$$t_{\max} = \underset{t\in\mathcal{T}}{\mathrm{argmax}}\ [\boldsymbol{d}_l]_t\,. \tag{91}$$

The SCA iterations are repeated until $\tilde{\boldsymbol{E}}$ converges. Once $\tilde{\boldsymbol{E}}^{\mathrm{opt}}$ is obtained, we can get $\boldsymbol{\pi}^{\mathrm{opt}}$ using (33).

After determining $\boldsymbol{\pi}^{\mathrm{opt}}$, we fix $(\boldsymbol{\pi}, \{\boldsymbol{\theta}_{\mathcal{N}_t}\}_{t=1}^{T}) = (\boldsymbol{\pi}^{\mathrm{opt}}, \{\boldsymbol{\theta}_{\mathcal{N}_t}^{\mathrm{opt}}\}_{t=1}^{T})$ and then optimize $\boldsymbol{\tau}$. By plugging (78) to (79), the time delay control problem $\tilde{\mathscr{P}}_{0,\mathrm{b}}$ is formulated as

$$\tilde{\mathscr{P}}_{0,\mathrm{b}}: \quad \underset{\boldsymbol{\tau}}{\text{maximize}} \quad \sum_{s=1}^{S} \left|\sum_{t=1}^{T} m_{s,t} e^{j v_{s,t}}\right|^2 [-3pt] \tag{92a}$$
$$\text{subject to} \quad v_{s,t} = \angle\left(\boldsymbol{a}_{N,t}^{\mathrm{H}}(\boldsymbol{p}, f_s)\, \boldsymbol{w}^{\mathrm{ps}}(\boldsymbol{\theta}_{\mathcal{N}_t})\right) - 2\pi f_s \tau_t \quad \forall s \in \mathcal{S}, t \in \mathcal{T}\,. \tag{92b}$$

As shown in Remark 1, $m_{s,t}$ is a sole function of $\boldsymbol{\theta}_{\mathcal{N}_t}$ and thus, is unaffected by $\boldsymbol{\tau}$. Thus, by redefining the optimization variable $\tilde{\boldsymbol{\tau}} = [\, e^{-jf_c\tau_1} \ e^{-jf_c\tau_2} \ \ldots \ e^{-jf_c\tau_T} \,]^{\mathrm{T}}$, $\tilde{\mathscr{P}}_{0,\mathrm{b}}$ can be recast to the unconstrained problem on $\mathcal{C}^T$ as

$$\tilde{\mathscr{P}}_{1,\mathrm{b}}: \quad \underset{\tilde{\boldsymbol{\tau}}\in\mathcal{C}^T}{\text{maximize}} \quad \sum_{s=1}^{S} \left|\boldsymbol{m}_s^{\mathrm{T}} \boldsymbol{P}_s \tilde{\boldsymbol{\tau}}^{\left(2\pi\frac{f_s}{f_c}\right)}\right|^2 \tag{93}$$

where $\boldsymbol{m}_s \in \mathbb{R}^T$ and $\boldsymbol{P}_s \in \mathbb{C}^{T\times T}$ are defined as

$$\boldsymbol{m}_s \triangleq [\, m_{s,1}\,, m_{s,2} \cdots m_{s,T} \,]^{\mathrm{T}} \tag{94}$$
$$\boldsymbol{P}_s \triangleq \mathrm{diag}\Big(e^{j\angle(\boldsymbol{a}_{N,1}^{\mathrm{H}}(\boldsymbol{p},f_s)\, \boldsymbol{w}^{\mathrm{ps}}(\boldsymbol{\theta}_{\mathcal{N}_1}))}, e^{j\angle(\boldsymbol{a}_{N,2}^{\mathrm{H}}(\boldsymbol{p},f_s)\, \boldsymbol{w}^{\mathrm{ps}}(\boldsymbol{\theta}_{\mathcal{N}_2}))}, \ldots, e^{j\angle(\boldsymbol{a}_{N,T}^{\mathrm{H}}(\boldsymbol{p},f_s)\, \boldsymbol{w}^{\mathrm{ps}}(\boldsymbol{\theta}_{\mathcal{N}_T}))}\Big)\,. \tag{95}$$

The near-optimal solution $\tilde{\boldsymbol{\tau}}^{\mathrm{opt}}$ of $\tilde{\mathscr{P}}_{1,\mathrm{b}}$ can be obtained via the RCG method. We then get $\tau_t^{\mathrm{opt}} = -\frac{1}{f_c}\angle\tilde{\tau}_t^{\mathrm{opt}}$ for all $t \in \mathcal{T}$.

C. Distributed Phase Shifts Control

Now, we explain the distributed phase shift control for optimizing $\{\boldsymbol{\theta}_{\mathcal{N}_t}\}_{t=1}^{T}$. For a given $(\boldsymbol{\pi}, \boldsymbol{\tau}) = (\boldsymbol{\pi}^{\mathrm{opt}}, \boldsymbol{\tau}^{\mathrm{opt}})$, $\tilde{\mathscr{P}}_0$ is reduced to the phase shift control problem $\tilde{\mathscr{P}}_{0,\mathrm{c}}$ as

$$\tilde{\mathscr{P}}_{0,\mathrm{c}}: \underset{\{\boldsymbol{\theta}_{\mathcal{N}_t}\}_{t=1}^{T}}{\text{maximize}} \quad \sum_{s=1}^{S} \left|\sum_{t=1}^{T} m_{s,t} e^{j v_{s,t}}\right|^2 \tag{96a}$$
$$\text{subject to} \quad m_{s,t} = \left|\boldsymbol{a}_{N,t}^{\mathrm{H}}(\boldsymbol{p}, f_s)\, \boldsymbol{w}^{\mathrm{ps}}(\boldsymbol{\theta}_{\mathcal{N}_t})\right| \quad \forall\, s \in \mathcal{S},\, t \in \mathcal{T} \tag{96b}$$
$$v_{s,t} = \angle\left(\boldsymbol{a}_{N,t}^{\mathrm{H}}(\boldsymbol{p}, f_s)\, \boldsymbol{w}^{\mathrm{ps}}(\boldsymbol{\theta}_{\mathcal{N}_t})\right) - 2\pi f_s \tau_t \quad \forall\, s \in \mathcal{S},\, t \in \mathcal{T}. \tag{96c}$$

Unfortunately, one cannot directly decompose $\tilde{\mathscr{P}}_{0,\mathrm{c}}$ into subproblems for each $\boldsymbol{\theta}_{\mathcal{N}_t}$ since (96a) is a joint function of $\{\boldsymbol{\theta}_{\mathcal{N}_t}\}_{t=1}^{T}$. To address this issue, we first determine $\{m_{s,t}, v_{s,t}\}_{s,t}$ that maximizes (96a) and then individually optimize each $\boldsymbol{\theta}_{\mathcal{N}_t}$ satisfying (96b) and (96c). First, by relaxing (96b) and (96c), the optimization problem $\tilde{\mathscr{P}}_{1,\mathrm{c}}$ for determining $\{m_{s,t}, v_{s,t}\}_{s,t}$ is formulated as

$$\tilde{\mathscr{P}}_{1,\mathrm{c}}: \quad \underset{\{m_{s,t}, v_{s,t}\}_{s,t}}{\text{maximize}} \quad \sum_{s=1}^{S} \left|\sum_{t=1}^{T} m_{s,t} e^{j v_{s,t}}\right|^2 \tag{97a}$$
$$\text{subject to} \quad 0 \leqslant m_{s,t} \leqslant |\mathcal{N}_t| \qquad \forall\, t \in \mathcal{T}\,. \tag{97b}$$

The optimal solutions $m_{s,t}^{\mathrm{opt}}$ and $v_{s,t}^{\mathrm{opt}}$ of $\tilde{\mathscr{P}}_{1,\mathrm{c}}$ are given by

$$m_{s,t}^{\mathrm{opt}} = |\mathcal{N}_t| \qquad \forall\, s \in \mathcal{S},\, t \in \mathcal{T} \tag{98}$$
$$v_{s,t}^{\mathrm{opt}} = x_s \qquad \forall\, s \in \mathcal{S},\, t \in \mathcal{T} \tag{99}$$

where $x_s \in [0, 2\pi)$ is the common argument of all subarray gains $\{G_t(\boldsymbol{w}_{s,t}, \boldsymbol{p})\}_{t=1}^{T}$ at the sth subcarrier.

Once we obtain $\{m_{s,t}^{\mathrm{opt}}, v_{s,t}^{\mathrm{opt}}\}_{s,t}$, we determine $\{\boldsymbol{\theta}_{\mathcal{N}_t}\}_{t=1}^{T}$ satisfying (96b) and (96c). Specifically, the corresponding optimization problem $\tilde{\mathscr{P}}_{2,\mathrm{c}}$ is formulated as

$$\tilde{\mathscr{P}}_{2,\mathrm{c}}: \underset{\boldsymbol{\theta}_{\mathcal{N}_t}, \{x_s\}_{s=1}^{S}}{\text{minimize}} \quad \sum_{s=1}^{S}\sum_{t=1}^{T} \left|\boldsymbol{a}_{N,t}^{\mathrm{H}}(\boldsymbol{p}, f_s)\, \boldsymbol{w}^{\mathrm{ps}}(\boldsymbol{\theta}_{\mathcal{N}_t}) - |\mathcal{N}_t| e^{j(2\pi f_s \tau_t + x_s)}\right|^2. \tag{100}$$

To solve $\tilde{\mathscr{P}}_{2,\mathrm{c}}$, we use the alternating approach comprising two steps: 1) common argument optimization that fixes $\{\boldsymbol{\theta}_{\mathcal{N}_t}\}_{t=1}^{T}$ and determines $\{x_s\}_{s=1}^{S}$; and 2) phase shift optimization that fixes $\{x_s\}_{s=1}^{S}$ and determines each $\boldsymbol{\theta}_{\mathcal{N}_t}$ separately.

1) Common Argument Optimization: For given $\{\boldsymbol{\theta}_{\mathcal{N}_t}\}_{t=1}^T$, $\tilde{\mathscr{P}}_{2,\mathrm{c}}$ is reduced to $\tilde{\mathscr{P}}_{3,\mathrm{c}}$ as

$$\tilde{\mathscr{P}}_{3,\mathrm{c}}: \underset{\{x_s\}_{s=1}^S}{\text{minimize}} \sum_{t=1}^T \sum_{s=1}^S \left| G_t(\boldsymbol{w}_{s,t}, \boldsymbol{p}) - |\mathcal{N}_t| e^{j(2\pi f_s \tau_t + x_s)} \right|^2. \tag{101}$$

Then, $\tilde{\mathscr{P}}_{3,c}$ can be decomposed into subproblems for each x_s:

$$\tilde{\mathscr{P}}_{3,\mathrm{c},s}: \quad \underset{x_s}{\text{minimize}} \quad \sum_{t=1}^T \left| G_t(\boldsymbol{w}_{s,t}, \boldsymbol{p}) - |\mathcal{N}_t| e^{j(2\pi f_s \tau_t + x_s)} \right|^2. \tag{102}$$

By redefining the variable $\tilde{x}_s \triangleq e^{jx_s} \in \mathcal{C}^1$ and the coefficient vectors $\boldsymbol{g}_s \triangleq [\, G_1(\boldsymbol{w}_{s,1}, \boldsymbol{p}) \; G_2(\boldsymbol{w}_{s,2}, \boldsymbol{p}) \cdots G_T(\boldsymbol{w}_{s,T}, \boldsymbol{p}) \,]^{\mathrm{T}}$ and $\boldsymbol{v}_s \triangleq [\, |\mathcal{N}_1| e^{j2\pi f_s \tau_1} \; |\mathcal{N}_2| e^{j2\pi f_s \tau_2} \cdots |\mathcal{N}_T| e^{j2\pi f_s \tau_T} \,]^{\mathrm{T}}$, $\tilde{\mathscr{P}}_{3,\mathrm{c},s}$ can be simplified as

$$\tilde{\mathscr{P}}_{4,\mathrm{c},s}: \quad \underset{\tilde{x}_s \in \mathcal{C}^1}{\text{minimize}} \quad \|\boldsymbol{g}_s - \boldsymbol{v}_s \tilde{x}_s\|_2^2 \,. \tag{103}$$

Since $\|\boldsymbol{g}_s - \boldsymbol{v}_s \tilde{x}_s\|_2^2 = \|\boldsymbol{g}_s\|_2^2 + \|\boldsymbol{v}_s\|_2^2 - 2\Re\{\tilde{x}_s^* \boldsymbol{v}_s^{\mathrm{H}} \boldsymbol{g}_s\}$, the optimal solution $\tilde{x}_s^{\mathrm{opt}}$ of $\tilde{\mathscr{P}}_{4,\mathrm{c},s}$ is given by

$$\tilde{x}_s^{\mathrm{opt}} = \underset{\tilde{x}_s \in \mathcal{C}^1}{\operatorname{argmax}} \; \Re\{\tilde{x}_s^* \boldsymbol{v}_s^{\mathrm{H}} \boldsymbol{g}_s\} = \frac{\boldsymbol{v}_s^{\mathrm{H}} \boldsymbol{g}_s}{|\boldsymbol{v}_s^{\mathrm{H}} \boldsymbol{g}_s|} \,. \tag{104}$$

Then, by extracting the complex argument from $\tilde{x}_s^{\mathrm{opt}}$, we can obtain the optimal common argument $x_s^{\mathrm{opt}} = \angle \tilde{x}_s^{\mathrm{opt}}$.

2) Phase Shift Optimization: For given $\{x_s\}_{s=1}^S$, $\tilde{\mathscr{P}}_{2,\mathrm{c}}$ is reduced to $\tilde{\mathscr{P}}_{3,\mathrm{c}}$ as

$$\tilde{\mathscr{P}}_{3,\mathrm{c}}: \quad \underset{\{\boldsymbol{\theta}_{\mathcal{N}_t}\}_{t=1}^T}{\text{minimize}} \quad \sum_{t=1}^T \sum_{s=1}^S \Big| \boldsymbol{a}_{N,t}^{\mathrm{H}}(\boldsymbol{p}, f_s)\, \boldsymbol{w}^{\mathrm{ps}}(\boldsymbol{\theta}_{\mathcal{N}_t}) - |\mathcal{N}_t| e^{j(2\pi f_s \tau_t + x_s)} \Big|^2. \tag{105}$$

Since (96b) and (96c) are sole functions of $\boldsymbol{\theta}_{\mathcal{N}_t}$, $\tilde{\mathscr{P}}_{3,\mathrm{c}}$ can be decoupled into subproblems for each $\boldsymbol{\theta}_{\mathcal{N}_t}$ as

$$\tilde{\mathscr{P}}_{3,\mathrm{c},t}: \quad \underset{\boldsymbol{\theta}_{\mathcal{N}_t}}{\text{minimize}} \quad \sum_{s=1}^S \Big| \boldsymbol{a}_{N,t}^{\mathrm{H}}(\boldsymbol{p}, f_s)\, \boldsymbol{w}^{\mathrm{ps}}(\boldsymbol{\theta}_{\mathcal{N}_t}) - |\mathcal{N}_t| e^{j(2\pi f_s \tau_t + x_s)} \Big|^2. \tag{106}$$

By redefining the optimization variable to $\tilde{\boldsymbol{\theta}}_{\mathcal{N}_t} = [e^{-j\theta_n} : n \in \mathcal{N}_t]^{\mathrm{T}} \in \mathbb{C}^{|\mathcal{N}_t|}$, we can reformulate $\tilde{\mathscr{P}}_{3,\mathrm{c},t}$ to an unconstrained problem $\tilde{\mathscr{P}}_{4,\mathrm{c},t}$ on $\mathcal{C}^{|\mathcal{N}_t|}$ as

$$\tilde{\mathscr{P}}_{4,\mathrm{c},t}: \underset{\tilde{\boldsymbol{\theta}}_{\mathcal{N}_t} \in \mathcal{C}^{|\mathcal{N}_t|}}{\text{minimize}} \sum_{s=1}^S \left| \boldsymbol{a}_{N,t}^{\mathrm{H}}(\boldsymbol{p}, f_s)\, \tilde{\boldsymbol{\theta}}_{\mathcal{N}_t} - |\mathcal{N}_t| e^{j(2\pi f_s \tau_t + x_s)} \right|^2. \tag{107}$$

Using the RCG method, we can determine the near-optimal solution $\tilde{\boldsymbol{\theta}}_{\mathcal{N}_t}^{\mathrm{opt}}$ of $\tilde{\mathscr{P}}_{3,\mathrm{c},t}$, from which we obtain $\theta_n^{\mathrm{opt}} = -\angle \tilde{\theta}_n^{\mathrm{opt}}$. The optimization of the common argument and phase shifts is iteratively performed until $\{\boldsymbol{\theta}_{\mathcal{N}_t}\}_{t=1}^T$ converge.

Finally, the dynamic subarray connection, time delay control, and phase shift control operations are repeated until $(\boldsymbol{\pi}, \boldsymbol{\tau}, \{\boldsymbol{\theta}_{\mathcal{N}_t}\}_{t=1}^T)$ converges. Algorithm 2 summarizes the distributed dynamic subarray connection and time delay/phase shift control algorithm.

Algorithm 2: Distributed Dynamic Subarray Connection and Time Delay/Phase Shift Control Algorithm.

Input: Target direction $\boldsymbol{p}$, subcarrier channel SNR $\{\rho_s\}_{s=1}^S$, the numbers of TTDs and PS subarrays T and L
Initialize: $\boldsymbol{\pi} = [\, 1\; 2 \cdots T \,]^{\mathrm{T}} \otimes \mathbf{1}_{L/T}$
    Set $\boldsymbol{\tau}$ and $\boldsymbol{\theta}$ as (12) and (13), respectively
while $(\boldsymbol{\pi}, \boldsymbol{\tau}, \boldsymbol{\theta})$ do not converge **do**
  $\tilde{\boldsymbol{E}}$ = Successive convex approximation ($\tilde{\mathscr{P}}_{1,\mathrm{a}}$)
  $\pi_l = \mathrm{supp}(\tilde{\boldsymbol{e}}_l)$ $\forall\, l \in \mathcal{L}$
  $\tilde{\boldsymbol{\tau}}$ = Riemannian conjugate gradient ($\mathcal{C}^T$, $\tilde{\mathscr{P}}_{1,\mathrm{b}}$)
  $\tau_t = \frac{1}{f_c} \angle \tilde{\tau}_t$ $\forall\, t \in \mathcal{T}$
  while $\{\boldsymbol{\theta}_{\mathcal{N}_t}\}_{t=1}^T$ do not converge **do**
   for $s = 1$ to S **do**
    Set $\boldsymbol{g}_s$ and $\boldsymbol{v}_s$ as (103)
    $\tilde{x}_s = \frac{\boldsymbol{v}_s^{\mathrm{H}} \boldsymbol{g}_s}{|\boldsymbol{v}_s^{\mathrm{H}} \boldsymbol{g}_s|}$, $x_s = \angle \tilde{x}_s$
   end for
   for $t = 1$ to T **do**
    $\tilde{\boldsymbol{\theta}}_{\mathcal{N}_t}$ = Riemannian conjugate gradient ($\tilde{\mathscr{P}}_{4,\mathrm{c},t}$)
    $\theta_n = \angle \tilde{\theta}_n$ $\forall n \in \mathcal{N}_t$
   end for
  end while
end while
Output: $\boldsymbol{\pi}$, $\boldsymbol{\tau}$, $\boldsymbol{\theta}$

Function Successive convex approximation ($\mathscr{P}$)
Set feasible initial starting point $\tilde{\boldsymbol{E}}$
while $\tilde{\boldsymbol{E}}$ do not converge **do**
  $\tilde{\boldsymbol{E}}^{\mathrm{prev}} = \tilde{\boldsymbol{E}}$
  Replace $f(\tilde{\boldsymbol{E}})$ with $F(\tilde{\boldsymbol{E}} \mid \tilde{\boldsymbol{E}}^{\mathrm{prev}})$
  Solve the relaxed problem
end while
Output: $\tilde{\boldsymbol{E}}$

V. Computational Complexity Analysis

In this section, we analyze the computational complexities of centralized and distributed WDAoSA schemes.

A. Complexity Analysis of Centralized WDAoSA Scheme

The centralized wideband beamforming optimization in Algorithm 1 consists of three major steps: 1) auxiliary variables (i.e., $\boldsymbol{\gamma}$ and $\boldsymbol{\nu}$) optimization via (27) and (28); 2) subarray connection vector (i.e., $\boldsymbol{\pi}$) optimization via RLA; and 3) TTD time delay and PS phase shift vectors (i.e., $\boldsymbol{\tau}$ and $\boldsymbol{\theta}$) optimization via RCG method. First, in the optimization step for $\boldsymbol{\gamma}$ and $\boldsymbol{\nu}$, the computational complexity of conducting (27) and (28) is $\mathcal{O}(NS)$. Second, in the optimization step for $\boldsymbol{\pi}$, the optimization problem is formulated as an SOCP (see (43)), which is solved by using the interior-point method. It has been shown that the computational complexity of the interior-point method for solving the SOCP problem with N_{var} variables is approximately $\mathcal{O}((N_{\mathrm{var}})^{3.5})$ [56]. Thus, the computational complexity of RLA is $\mathcal{O}((TL)^{3.5})$. Lastly, in the optimization step for $\boldsymbol{\tau}$ and $\boldsymbol{\theta}$, one can see that all operations of the RCG method are vector and matrix multiplication operations. Thus, the computational complexity of the RCG method is $\mathcal{O}(STN^2)$. In conclusion, the

TABLE I
COMPUTATIONAL COMPLEXITY COMPARISON

	Computational complexity
Centralized WDAoSA	$\mathcal{O}(STN^2 + (TL)^{3.5})$
Distributed WDAoSA	$\mathcal{O}(SN + S(T^2 + P^2))$
FDA	$\mathcal{O}(SN^3)$
DS-FTTD	$\mathcal{O}(SNT)$
PDF	$\mathcal{O}(N)$
PS-based beamforming	$\mathcal{O}(N)$

overall computational complexity of the centralized WDAoSA scheme is $\mathcal{O}(STN^2 + (TL)^{3.5})$.

B. Complexity Analysis of Distributed WDAoSA Scheme

The distributed wideband beamforming optimization in Algorithm 2 consists of three major steps: 1) $\boldsymbol{\pi}$ optimization via SCA; 2) $\boldsymbol{\tau}$ optimization via RCG method; and 3) $\{\boldsymbol{\theta}_{\mathcal{N}_t}\}_{t=1}^{T}$ optimizations via RCG method. Note that in this algorithm, the optimization variables are updated by the closed-form solutions. First, in the optimization step for $\boldsymbol{\pi}$, the computational complexity of vector multiplication is $\mathcal{O}(NS)$. Second, in the optimization step for $\boldsymbol{\tau}$, the computational complexity of RCG method is $\mathcal{O}(T^2S)$. Finally, in the optimization step for each $\boldsymbol{\theta}_{\mathcal{N}_t}$, the computational complexity of RCG method is approximately $\mathcal{O}(P^2S)$ where $P = \frac{N}{T}$. In conclusion, the overall computational complexity of the distributed WDAoSA scheme is $\mathcal{O}(SN + S(T^2 + P^2))$. Note that while the computational complexity of the centralized approach scales with N^2, that of the distributed approach scales with N, meaning that the distributed approach can effectively reduce computational complexity in ELAA systems. In Table I, we compare the computational complexity of the WDAoSA with that of the conventional partially-connected beamforming schemes.

VI. NUMERICAL RESULTS

In this section, we present numerical results to validate the effectiveness of the proposed WDAoSA scheme for both centralized and distributed approaches.

A. Simulation Setup

In our simulations, we consider the wideband THz ELAA systems where a BS equipped with $N = 64 \times 4$ URA antennas serves a single-antenna UE by generating frequency-dependent beams $\{\boldsymbol{w}_s\}_{s=1}^{S}$ directed towards the UE position $\boldsymbol{p}^{\mathrm{ue}}$. We consider the 3D coordinate system where the BS antenna array is located at the XY-plane. The UE is located randomly around the BS within the cell radius of $R = 20\,\mathrm{m}$. Additionally, the scatterers are randomly distributed around the UE. We set the numbers of TTDs and PS subarrays to $T = 4$ and $L = 64$, respectively. The time delays and phase shifts of the TTDs and PSs can vary continuously within the ranges $[0, \frac{N}{2f_c})$ for the TTDs and $[0, 2\pi)$ for the PSs, respectively [32], [37]. Note that the number of PSs is the same as the number of antennas N, so each PS subarray consists of $K = \frac{N}{L} = 4$ PSs. We use the frequency-selective geometric THz channel model

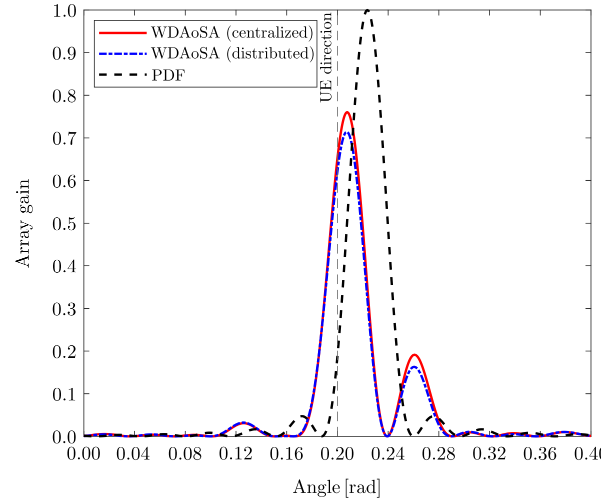

Fig. 2. Array gain as a function of the angle.

where the carrier frequency is $f_c = 100\,\mathrm{GHz}$, the bandwidth is $B = 20\,\mathrm{GHz}$, and the number of subcarriers is $S = 128$. These frequency-domain system parameters are chosen to set the frequency granularity of the proposed WDAoSA scheme. We set the subcarrier frequencies to $f_s = f_c - \frac{B}{2} + \frac{B(s-1)}{S-1}$. The number of propagation paths is $N_p = 4$ and the path loss and path gain are modeled as $\beta_s = (\frac{c}{4\pi f_s r})^2 e^{-k(f_s)r}$ and $\alpha_{s,i} \sim \mathcal{CN}(0, \Gamma_i(f_s))$ where $k(f_s)$ and $\Gamma_i(f_s)$ are defined in [37] and [41], respectively. Throughout the simulation, we set the SNR to $\rho_s = \frac{\beta_s N P_{\mathrm{tx}}}{\sigma^2} = 10\,\mathrm{dB}$ for all subcarriers. As performance metrics, we use the sum of squares of array gains $G_{\mathrm{sum}} = \frac{1}{N^2}\sum_{s=1}^{S} |\boldsymbol{a}_N^{\mathrm{H}}(\boldsymbol{p}, f_s)\, \boldsymbol{w}_s|^2$, the sum of logarithms of array gains $G_{\mathrm{tot}} = \sum_{s=1}^{S} \log_2(1 + \frac{\rho_s}{N^2}|\boldsymbol{a}_N^{\mathrm{H}}(\boldsymbol{p}, f_s)\, \boldsymbol{w}_s|^2)$, and the spectral efficiency $\mathsf{R} = \frac{1}{S}\sum_{s=1}^{S} \log_2(1 + \frac{P_{\mathrm{tx}}}{\sigma^2}|\mathbf{h}_s^{\mathrm{H}} \boldsymbol{w}_s|^2)$.

For comparison, we use four partially-connected beamforming schemes: 1) fully-digital approximation (FDA) scheme which optimizes $\boldsymbol{\tau}$ and $\boldsymbol{\theta}$ iteratively [37]; 2) dynamic-subarray with fixed TTD (DS-FTTD) scheme which uses the dynamic subarray architecture between TTDs and PSs with fixed TTD time delays [38]; 3) phase-delay focusing (PDF) scheme which controls the TTD time delays and PS phase shifts as (12) and (13) [36]; and 4) PS-based beamforming scheme which generates the frequency-invariant beamforming vectors.

B. Simulation Results

In Fig. 2, we locate the UE at $(r^{\mathrm{ue}}, \theta^{\mathrm{ue}}, \phi^{\mathrm{ue}}) = (12\,\mathrm{m}, 0.2\,\mathrm{rad}, 0.2\,\mathrm{rad})$ and plot the power of the array gain $|G(\boldsymbol{w}_1, \boldsymbol{p})|^2 = \frac{1}{N^2}|\boldsymbol{a}_N^{\mathrm{H}}(\boldsymbol{p}, f_1)\, \boldsymbol{w}_1|^2$ at the first subcarrier as a function of the azimuth angle ϕ of $\boldsymbol{p} = [\, r\sin\theta\cos\phi \; r\sin\theta\sin\phi \; r\cos\theta\,]^{\mathrm{T}}$ while fixing $r = r^{\mathrm{ue}}$ and $\theta = \theta^{\mathrm{ue}}$. We observe that both the centralized and distributed WDAoSA achieve an array gain of 0.7 near the UE direction (i.e., $\phi^{\mathrm{ue}} = 0.2\,\mathrm{rad}$). Considering that the difference between f_1 and f_c is almost 10 GHz, this notable array gain enhancement capability of WDAoSA is somewhat surprising. We also observe that the beam direction of the proposed WDAoSA scheme closely matches the UE direction, whereas the beam direction of the conventional PDF scheme is clearly misaligned with the UE direction. When the number of TTDs is small,

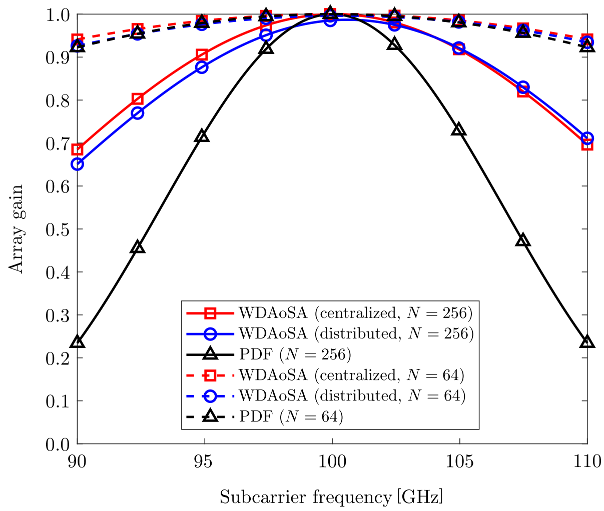

Fig. 3. Array gain as a function of the subcarrier frequency.

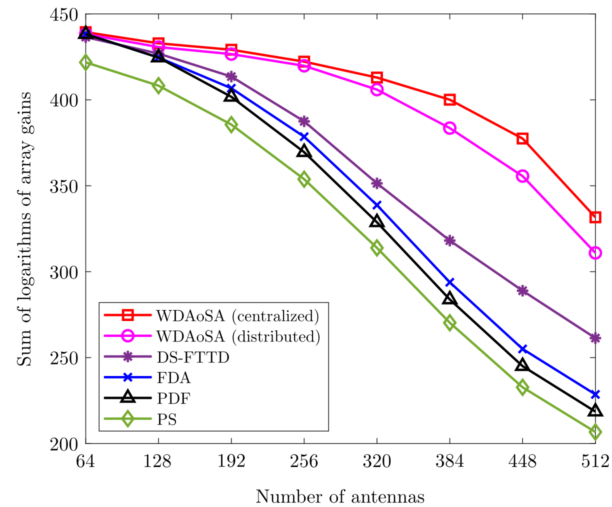

Fig. 5. Sum of logarithms of array gains as a function of the number of antennas.

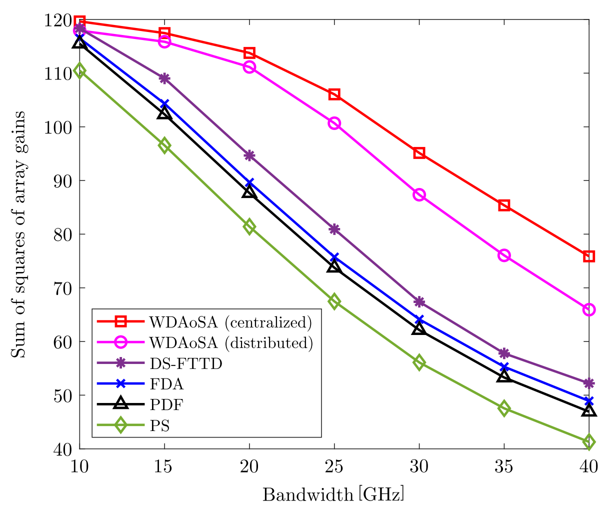

Fig. 4. Sum of squares of array gains as a function of the system bandwidth.

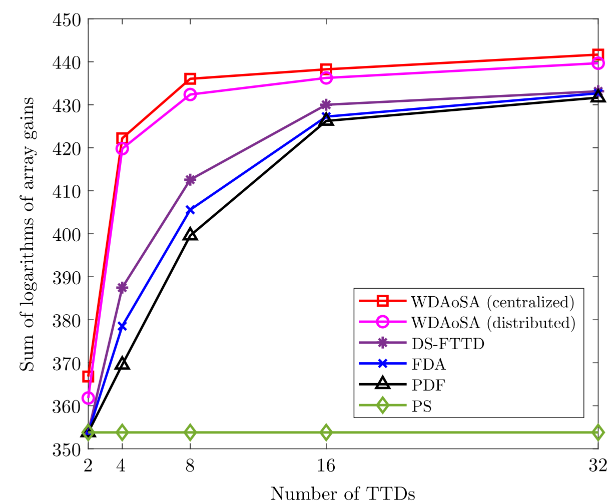

Fig. 6. Sum of logarithms of array gains as a function of the number of TTDs.

the subcarrier beams of the conventional partially-connected structure become similar to the PS beams and fail to focus the beam directions on the UE. On the other hand, by utilizing the dynamic subarray connection and optimized time delay and phase shift control operations, WDAoSA effectively maximizes the array gain at the UE direction, thereby mitigating the beam squint effect.

Fig. 3 shows the power of the array gain $|G(\boldsymbol{w}_s, \boldsymbol{p})|^2$ as a function of the subcarrier frequency f_s for various numbers of antennas, while maintaining the UE position at $(r^{\text{ue}}, \theta^{\text{ue}}, \phi^{\text{ue}}) = (12\,\text{m}, 0.2\,\text{rad}, 0.2\,\text{rad})$. We observe that for a relatively small number of antennas (e.g., $N = 64$), the array gain degradation caused by the beam squint effect is marginal. However, for a larger number of antennas (e.g., $N = 256$), the array gains of the conventional TTD-based beamforming schemes decrease sharply as $|f_s - f_\text{c}|$ increases. For example, when $f_s = 90\,\text{GHz}$, the FDA scheme experiences an array gain loss of nearly 70% compared to the maximum array gain of 1. On the other hand, the array gain loss of the centralized WDAoSA scheme is less than 30%, meaning that it achieves more than 40% array gain improvement over the FDA scheme. This is because WDAoSA flexibly adjusts the connections between TTDs and PS subarrays to reduce the discrepancy between the optimal beams and the generated beams but the FDA scheme has no such mechanism to improve the array gains of the subcarrier beams.

Fig. 4 shows the sum of squares of array gains G_{sum} as a function of the system bandwidth B. We observe that the proposed WDAoSA scheme achieves significant array gain improvement over the conventional TTD-based beamforming schemes. We also observe that the array gain improvement of WDAoSA increases with the system bandwidth. For instance, when $B = 20\,\text{GHz}$, the array gain improvement of distributed WDAoSA over FDA scheme is around 24% but it rises to 35% when $B = 40\,\text{GHz}$. When the bandwidth increases, the difference between the carrier and subcarrier also increases, leading to a larger discrepancy between the optimal beams and the generated beams. While WDAoSA flexibly adjusts the

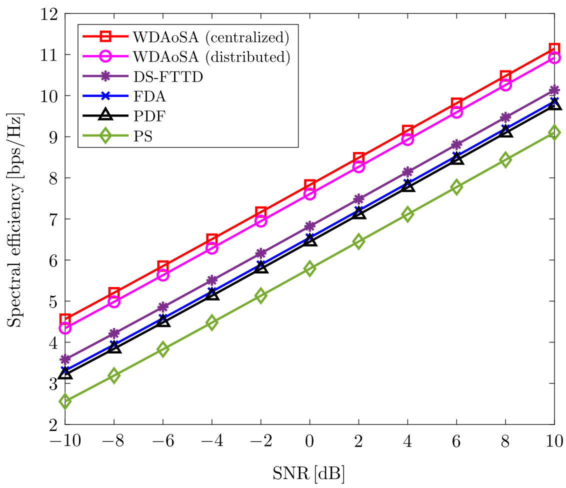

Fig. 7. Spectral efficiency as a function of SNR.

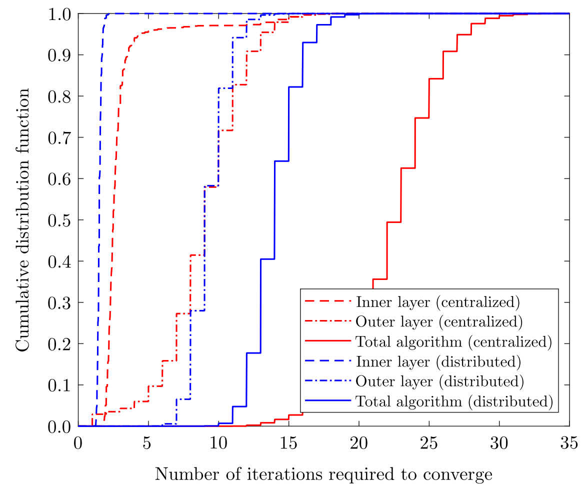

Fig. 9. Cumulative distribution of the number of iterations required to converge.

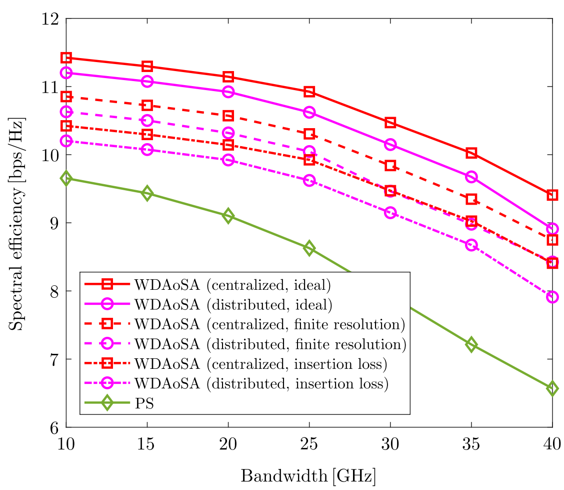

Fig. 8. Spectral efficiency as a function of the system bandwidth.

connections between TTDs and PS subarrays to minimize this discrepancy, FDA scheme has no such mechanism so the array gain degradation is unavoidable.

Fig. 5 shows the sum of logarithms of array gains G_{tot} as a function of the number of antennas N. We see that both the centralized and distributed WDAoSA schemes achieve higher array gain performance compared to the conventional TTD-based beamforming schemes across all tested regimes. In fact, we observe that the array gain improvement of WDAoSA increases with the number of antennas. Specifically, WDAoSA performs similar to other schemes when $N = 64$, but it achieves more than 27% improvement in array gain over the DS-FTTD scheme when $N = 512$. This is because the DS-FTTD scheme utilizes TTDs with fixed time delays, making it insufficient to prevent the array gain degradation in ELAA systems caused by the use of a limited number of TTDs. However, such is not the case for WDAoSA since it optimizes not only the subarray connections but also the TTD time delays and PS phase shifts.

Fig. 6 shows the sum of logarithms of array gains G_{tot} as a function of the number of TTDs T. We observe that the proposed WDAoSA scheme substantially enhances the array gain compared to conventional partially-connected beamforming schemes. In particular, the array gain enhancement of the WDAoSA increases as T decreases. When the number of TTDs is small, the conventional partially-connected beamforming schemes cannot effectively mitigate the beam squint effect, causing a misalignment between the subcarrier beam directions and the UE direction (see Fig. 2). This implies that in wideband ELAA systems where the number of antennas greatly exceeds the number of TTDs, the WDAoSA can be an effective solution for the beamforming vector generation.

Fig. 7 shows the spectral efficiency as a function of SNR ρ_s. We observe that the proposed WDAoSA scheme outperforms the conventional partially-connected beamforming schemes. For example, when $SNR = 0\,\text{dB}$, the centralized WDAoSA achieves around 14%, 16%, and 24% spectral efficiency gains over the FDA, PDF, and PS-based beamforming schemes, respectively. Even when compared with the DS-FTTD scheme, the spectral efficiency gain of WDAoSA is around 10%. This notable spectral efficiency performance of WDAoSA is attributed to two key factors: 1) the power of mmWave and THz band signals is mostly concentrated along the LoS path; and 2) WDAoSA generates sharp beams that are precisely directed towards the UE.

To demonstrate the effectiveness of the proposed WDAoSA scheme in real-world systems, the spectral efficiency performance under various practical constraints is shown in Fig. 8. These include the insertion losses of TTDs and switches and the finite resolutions of TTDs and PSs. Specifically, we set the insertion losses of switches and TTDs to 2 dB and 1 dB, respectively, and then incorporate these losses in the spectral efficiency calculations [57]. Additionally, the continuous values of TTD time delays and PS phase shifts obtained from the WDAoSA are quantized using 9-bit uniform codebooks [58]. We observe that even with these insertion losses, the WDAoSA achieves significant spectral efficiency gain over the traditional PS-based beamforming scheme. We also observe that while spectral efficiency is slightly reduced due to quantization, the overall impact remains minimal.

Fig. 9 shows the cumulative distributions of the number of iterations needed for the convergence of WDAoSA. Note that the inner layer of the centralized WDAoSA scheme includes the RLA-based subarray connection vector optimization and the RCG-based time delay/phase shift optimization (see Algorithm 1). Also, the inner layer of the distributed WDAoSA scheme includes the SCA-based subarray connection vector optimization and the RCG-based time delay/phase shift optimization (see Algorithm 2). We observe that both algorithms converge within 30 iterations.

VII. Conclusion

In this paper, we proposed a TTD-based wideband beamforming architecture called WDAoSA that dynamically reconfigures the connections between TTDs and PS subarrays using a switch network. While the beam misalignment and array gain degradation of subcarrier beams are unavoidable in the conventional TTD-based beamforming schemes due to the fixed subarray connection, such is not the case for WDAoSA since the subarray connection as well as the TTD time delays and PS phase shifts are deliberately optimized to maximize the array gain. Specifically, we developed both centralized and distributed beamforming optimization techniques that jointly fine-tune the subarray connections, TTD time delays, and PS phase shifts. From the numerical evaluations, we demonstrated that WDAoSA achieves more than 40% array gain improvement over the conventional TTD-based beamforming schemes. In our work, we restricted our attention to wideband ELAA systems, but we believe that there are many research extensions of WDAoSA including reconfigurable intelligent surfaces (RIS)-aided systems and non-terrestrial networks (NTN).

Appendix
Proof of Proposition 1

Proof: Since f_1 is a concave differentiable function of $\boldsymbol{\nu}$, $\boldsymbol{\nu}^{\mathrm{opt}}$ in (28) can be obtained by solving $\frac{\partial f_1}{\partial \boldsymbol{\nu}} = \mathbf{0}_S$. Then, for a given $\boldsymbol{\nu} = \boldsymbol{\nu}^{\mathrm{opt}}$, f_1 is expressed as

$$f_1(\boldsymbol{\pi}, \boldsymbol{\tau}, \boldsymbol{\theta}, \boldsymbol{\gamma}, \boldsymbol{\nu}^{\mathrm{opt}}) = \sum_{s=1}^{S} \log_2(1+\gamma_s) - \sum_{s=1}^{S} \gamma_s + \sum_{s=1}^{S} \frac{(1+\gamma_s)\rho_s \left|\boldsymbol{a}_N^{\mathrm{H}}(\boldsymbol{p}, f_s)\, \boldsymbol{w}_s\right|^2}{\rho_s \left|\boldsymbol{a}_N^{\mathrm{H}}(\boldsymbol{p}, f_s)\, \boldsymbol{w}_s\right|^2 + N^2}. \tag{108}$$

Similarly, f_1 in (108) is a concave differentiable function of $\boldsymbol{\gamma}$ so $\boldsymbol{\gamma}^{\mathrm{opt}}$ in (27) can be obtained by solving $\frac{\partial f_1}{\partial \boldsymbol{\gamma}} = \mathbf{0}_S$. Finally, by plugging $\boldsymbol{\nu}^{\mathrm{opt}}$ and $\boldsymbol{\gamma}^{\mathrm{opt}}$ to f_1, we get

$$f_1(\boldsymbol{\pi}, \boldsymbol{\tau}, \boldsymbol{\theta}, \boldsymbol{\gamma}^{\mathrm{opt}}, \boldsymbol{\nu}^{\mathrm{opt}}) = \sum_{s=1}^{S} \log_2\left(1 + \frac{\rho_s}{N^2}\left|\boldsymbol{a}_N^{\mathrm{H}}(\boldsymbol{p}, f_s)\, \boldsymbol{w}_s\right|^2\right). \tag{109}$$

Thus, $\mathscr{P}_0$ and $\mathscr{P}_1$ are equivalent in the sense that their optimal values are the same and $(\boldsymbol{\pi}, \boldsymbol{\tau}, \boldsymbol{\theta})$ is the optimal solution of $\mathscr{P}_0$ if and only if it is the optimal solution of $\mathscr{P}_1$.

Acknowledgment

The authors wish to thank A. Conti and C. A. Gómez-Vega for their helpful suggestions and careful reading of the manuscript.

References

[1] Z. Wang et al., "A tutorial on extremely large-scale MIMO for 6G: Fundamentals, signal processing, and applications," *IEEE Commun. Surveys Tuts.*, vol. 26, no. 3, pp. 1560–1605, 3rd Quart. 2024.

[2] E. G. Larsson, O. Edfors, F. Tufvesson, and T. L. Marzetta, "Massive MIMO for next generation wireless systems," *IEEE Commun. Mag.*, vol. 52, no. 2, pp. 186–195, Feb. 2014.

[3] Y. Shen and M. Z. Win, "Fundamental limits of wideband localization–Part I: A general framework," *IEEE Trans. Inf. Theory*, vol. 56, no. 10, pp. 4956–4980, Oct. 2010.

[4] P. Yang, Y. Xiao, M. Xiao, and S. Li, "6G wireless communications: Vision and potential techniques," *IEEE Netw.*, vol. 33, no. 4, pp. 70–75, Jul./Aug. 2019.

[5] L. Lu, G. Y. Li, A. L. Swindlehurst, A. Ashikhmin, and R. Zhang, "An overview of massive MIMO: Benefits and challenges," *IEEE J. Sel. Topics Signal Process.*, vol. 8, no. 5, pp. 742–758, Oct. 2014.

[6] Y. Shen and M. Z. Win, "On the accuracy of localization systems using wideband antenna arrays," *IEEE Trans. Commun.*, vol. 58, no. 1, pp. 270–280, Jan. 2010.

[7] R. Mendrzik, F. Meyer, G. Bauch, and M. Z. Win, "Enabling situational awareness in millimeter wave massive MIMO systems," *IEEE J. Sel. Topics Signal Process.*, vol. 13, no. 5, pp. 1196–1211, Sep. 2019.

[8] C. Han and Y. Chen, "Propagation modeling for wireless communications in the terahertz band," *IEEE Commun. Mag.*, vol. 56, no. 6, pp. 96–101, Jun. 2018.

[9] G. Kwon, H. Park, and M. Z. Win, "Joint beamforming and power splitting for wideband millimeter wave SWIPT systems," *IEEE J. Sel. Topics Signal Process.*, vol. 15, no. 5, pp. 1211–1227, Aug. 2021.

[10] G. J. Foschini, G. D. Golden, R. A. Valenzuela, and P. W. Wolniansky, "Simplified processing for high spectral efficiency wireless communication employing multi-element arrays," *IEEE Trans. Commun.*, vol. 17, no. 11, pp. 1841–1852, Nov. 1999.

[11] E. A. Jorswieck and H. Boche, "Channel capacity and capacity-range of beamforming in MIMO wireless systems under correlated fading with covariance feedback," *IEEE Trans. Wireless Commun.*, vol. 3, no. 5, pp. 1543–1553, Sep. 2004.

[12] A. Giorgetti, M. Chiani, and M. Z. Win, "The effect of narrowband interference on wideband wireless communication systems," *IEEE Trans. Commun.*, vol. 53, no. 12, pp. 2139–2149, Dec. 2005.

[13] J. H. Winters, "Optimum combining in digital mobile radio with cochannel interference," *IEEE J. Sel. Areas Commun.*, vol. SAC-2, no. 4, pp. 528–539, Jul. 1984.

[14] A. Conti, W. M. Gifford, M. Z. Win, and M. Chiani, "Optimized simple bounds for diversity systems," *IEEE Trans. Commun.*, vol. 57, no. 9, pp. 2674–2685, Sep. 2009.

[15] J. H. Winters, "On the capacity of radio communication systems with diversity in Rayleigh fading environment," *IEEE J. Sel. Areas Commun.*, vol. 5, no. 5, pp. 871–878, Jun. 1987.

[16] G. J. Foschini, "Layered space–time architecture for wireless communication in a fading environment when using multi-element antennas," *Bell Labs Tech. J.*, vol. 1, no. 2, pp. 41–59, Autumn 1996.

[17] A. Conti et al., "Location awareness in beyond 5G networks," *IEEE Commun. Mag.*, vol. 59, no. 11, pp. 22–27, Nov. 2021.

[18] W. M. Gifford, M. Z. Win, and M. Chiani, "On the SNR penalty for antenna subset diversity," in *Proc. Int. Wireless Commun. Mobile Comput.*, Vancouver, Canada, Jul. 2006, pp. 617–622.

[19] J. H. Winters, J. Salz, and R. D. Gitlin, "The impact of antenna diversity on the capacity of wireless communication system," *IEEE Trans. Commun.*, vol. 42, no. 234, pp. 1740–1751, Feb./Mar/Apr. 1994.

[20] P. F. Driessen and G. J. Foschini, "On the capacity formula for multiple input-multiple output wireless channels: A geometric interpretation," *IEEE Trans. Commun.*, vol. 47, no. 2, pp. 173–176, Feb. 1999.

[21] J. H. Winters, "Optimum combining for indoor radio systems with multiple users," *IEEE Trans. Commun.*, vol. 35, no. 11, pp. 1222–1230, Nov. 1987.

[22] M. Z. Win, N. C. Beaulieu, L. A. Shepp, B. F. Logan, and J. H. Winters, "On the SNR penalty of MPSK with hybrid selection/maximal ratio combining over IID Rayleigh fading channels," *IEEE Trans. Commun.*, vol. 51, no. 6, pp. 1012–1023, Jun. 2003.

[23] M. Chiani, M. Z. Win, and H. Shin, "MIMO networks: The effects of interference," *IEEE Trans. Inf. Theory*, vol. 56, no. 1, pp. 336–349, Jan. 2010.

[24] T.-H. Chang, W.-C. Chiang, Y.-W. P. Hong, and C.-Y. Chi, "Training sequence design for discriminatory channel estimation in wireless MIMO systems," *IEEE Trans. Signal Process.*, vol. 58, no. 12, pp. 6223–6237, Dec. 2010.

[25] Y. Ahn et al., "Towards intelligent millimeter and terahertz communication for 6G: Computer vision-aided beamforming," *IEEE Wireless Commun.*, vol. 30, no. 5, pp. 179–186, Oct. 2023.
[26] C. Han et al., "Terahertz wireless channels: A holistic survey on measurement, modeling, and analysis," *IEEE Commun. Surv. Tuts.*, vol. 24, no. 3, pp. 1670–1707, thirdquarter 2022.
[27] B. Ning et al., "Beamforming technologies for ultra-massive MIMO in terahertz communications," *IEEE Open J. Commun. Soc.*, vol. 4, pp. 614–658, 2023.
[28] B. Wang, F. Gao, S. Jin, H. Lin, and G. Y. Li, "Spatial-and frequency-wideband effects in millimeter-wave massive MIMO systems," *IEEE Trans. Signal Process.*, vol. 66, no. 13, pp. 3393–3406, Jul. 2018.
[29] B. Wang, M. Jian, F. Gao, G. Y. Li, and H. Lin, "Beam squint and channel estimation for wideband mmWave massive MIMO-OFDM systems," *IEEE Trans. Signal Process.*, vol. 67, no. 23, pp. 5893–5908, Dec. 2019.
[30] H. Hashemi, T.-S. Chu, and J. Roderick, "Integrated true-time-delay-based ultra-wideband array processing," *IEEE Commun. Mag.*, vol. 46, no. 9, pp. 162–172, Sep. 2008.
[31] K. Spoof, V. Unnikrishnan, M. Zahra, K. Stadius, M. Kosunen, and J. Ryynänen, "True-time-delay beamforming receiver with RF re-sampling," *IEEE Trans. Circuits Syst. I, Reg. Papers*, vol. 67, no. 12, pp. 4457–4469, Dec. 2020.
[32] L. Dai, J. Tan, Z. Chen, and H. V. Poor, "Delay-phase precoding for wideband THz massive MIMO," *IEEE Trans. Wireless Commun.*, vol. 21, no. 9, pp. 7271–7286, Sep. 2022.
[33] S. Kim, J. Park, J. Moon, and B. Shim, "Fast and accurate terahertz beam management via frequency-dependent beamforming," *IEEE Trans. Wireless Commun.*, vol. 23, no. 3, pp. 1699–1712, Mar. 2024.
[34] F. Gao, B. Wang, C. Xing, J. An, and G. Y. Li, "Wideband beamforming for hybrid massive MIMO terahertz communications," *IEEE J. Sel. Areas Commun.*, vol. 39, no. 6, pp. 1725–1740, Jun. 2021.
[35] D. Q. Nguyen and T. Kim, "Joint delay and phase precoding under true-time delay constraints for THz massive MIMO," in *Proc. IEEE Int. Conf. Commun.*, May 2022, pp. 3496–3501.
[36] M. Cui and L. Dai, "Near-field wideband beamforming for extremely large antenna arrays," *IEEE Trans. Wireless Commun.*, vol. 23, no. 10, pp. 13110–13124, Oct. 2024.
[37] Z. Wang, X. Mu, and Y. Liu, "Beamfocusing optimization for near-field wideband multi-user communications," *IEEE Trans. Commun.*, vol. 73, no. 1, pp. 555–572, Jan. 2025.
[38] L. Yan, C. Han, and J. Yuan, "Energy-efficient dynamic-subarray with fixed true-time-delay design for terahertz wideband hybrid beamforming," *IEEE J. Sel. Areas Commun.*, vol. 40, no. 10, pp. 2840–2854, Oct. 2022.
[39] J. Wu, S. Kim, and B. Shim, "Parametric sparse channel estimation for RIS-assisted terahertz systems," *IEEE Trans. Commun.*, vol. 71, no. 9, pp. 5503–5518, Sep. 2023.
[40] I. E. Gordon et al., "The HITRAN2020 molecular spectroscopic database," *J. Quant. Spectrosc. Radiat. Transf.*, vol. 277, Jan. 2022, Art. no. 107949.
[41] S. Kim, J. Moon, J. Wu, B. Shim, and M. Z. Win, "Vision-aided positioning and beam focusing for 6G terahertz communications," *IEEE J. Sel. Areas Commun.*, vol. 42, no. 9, pp. 2503–2519, Sep. 2024.
[42] R. Piesiewicz, C. Jansen, D. Mittleman, T. Kleine-Ostmann, M. Koch, and T. Kurner, "Scattering analysis for the modeling of THz communication systems," *IEEE Trans. Antennas Propag.*, vol. 55, no. 11, pp. 3002–3009, Nov. 2007.
[43] J. A. Zhang, X. Huang, V. Dyadyuk, and Y. J. Guo, "Massive hybrid antenna array for millimeter-wave cellular communications," *IEEE Wireless Commun.*, vol. 22, no. 1, pp. 79–87, Feb. 2015.
[44] W. Zhang et al., "A grating-lobes suppression method for wideband MIMO millimeter-wave imaging arrays," *IEEE Trans. Antennas Propag.*, vol. 71, no. 2, pp. 1851–1862, Feb. 2023.
[45] *Study on New Radio Access Technology - Physical Layer Aspects (Release 14), 3rd Generation Partnership Project 3GPP^{TM}* TR 38.802 V14.2.0, Aug. 2017, release 14.
[46] Y.-N. R. Li, B. Gao, X. Zhang, and K. Huang, "Beam management in millimeter-wave communications for 5G and beyond," *IEEE Access*, vol. 8, pp. 13282–13293, 2020.
[47] E. J. Candes, M. B. Wakin, and S. P. Boyd, "Enhancing sparsity by reweighted l_1 minimization," *J. Fourier Anal. Appl.*, vol. 14, no. 5-6, pp. 877–905, Oct. 2008.
[48] S. Kim and B. Shim, "Energy-efficient millimeter-wave cell-free systems under limited feedback," *IEEE Trans. Commun.*, vol. 69, no. 6, pp. 4067–4082, Jun. 2021.
[49] K.-C. Toh, M. J. Todd, and R. H. Tütüncü, "SDPT3—a MATLAB software package for semidefinite programming, version 1.3," *Optim. Methods Softw.*, vol. 11, no. 1–4, pp. 545–581, 1999.
[50] J. Wu, S. Kim, and B. Shim, "Energy-efficient power control and beamforming for reconfigurable intelligent surface-aided uplink IoT networks," *IEEE Trans. Wireless Commun.*, vol. 21, no. 12, pp. 10162–10176, Dec. 2022.
[51] H. Sato, "Riemannian conjugate gradient methods: General framework and specific algorithms with convergence analyses," *SIAM J. Optim.*, vol. 32, no. 4, pp. 2690–2717, Dec. 2022.
[52] J. M. Lee, *Manifolds and Differential Geometry*. Providence, RI, USA: American Mathematical Society, 2022, vol. 107.
[53] P.-A. Absil, R. Mahony, and R. Sepulchre, *Optimization Algorithms on Matrix Manifolds*. Princeton, NJ, USA: Princeton Univ. Press, 2009.
[54] W. W. Hager and H. Zhang, "A new conjugate gradient method with guaranteed descent and an efficient line search," *SIAM J. Optim.*, vol. 16, no. 1, pp. 170–192, Jan. 2005.
[55] Y.-H. Dai and Y.-x. Yuan, *Nonlinear Conjugate Gradient Methods*. Shanghai, China: Shanghai Scientific and Technical Publishers, 2000.
[56] Y. Ye, *Interior Point Algorithms: Theory and Analysis*. Hoboken, NJ, USA: Wiley, 2011.
[57] Z. Wang, X. Mu, Y. Liu, and R. Schober, "TTD configurations for near-field beamforming: Parallel, serial, or hybrid?," *IEEE Trans. Commun.*, vol. 72, no. 6, pp. 545–581, Jun. 2024.
[58] D. Q. Nguyen, A. Ashikhmin, H. Yang, and T. Kim, "No analog combiner TTD-Based hybrid precoding for multi-user sub-THz communications," in *Proc. IEEE Int. Conf. Commun.*, Jun. 2024, pp. 1813–1818.

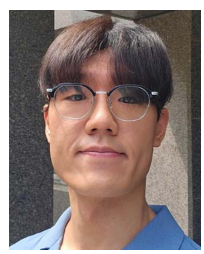

Seungnyun Kim (Member, IEEE) received the B.S. (with Hons.) and Ph.D. degrees in electrical and computer engineering from Seoul National University (SNU), Seoul, South Korea, in 2016 and 2023, respectively. He is currently a Postdoctoral Fellow with the Wireless Information and Network Sciences Laboratory, Massachusetts Institute of Technology, Cambridge, MA, USA.

His research interests include information theory, optimization methods, and machine learning with applications to real-world problems, including wireless communications, network localization and navigation, and nonterrestrial networks.

Dr. Kim was a recipient of the Sejong Science Fellowship from Korean Government in 2023, the Best Ph.D. Dissertation Award from SNU in 2023, the Qualcomm Innovation Fellowship Finalist in 2021, and the Samsung Humantech Paper Award Gold Prize in 2019.

Moe Z. Win (Fellow, IEEE) is the Robert R. Taylor Professor at the Massachusetts Institute of Technology (MIT) and the founding director of the Wireless Information and Network Sciences Laboratory. Prior to joining MIT, he was with AT&T Research Laboratories and with the NASA Jet Propulsion Laboratory.

His research encompasses fundamental theories, algorithm design, and network experimentation for a broad range of real-world problems. His current research topics include ultra-wideband systems, network localization and navigation, network interference exploitation, and quantum information science. He has served the IEEE Communications Society as an elected Member-at-Large on the Board of Governors, as elected Chair of the Radio Communications Committee, and as an IEEE Distinguished Lecturer. Over the last two decades, he held various editorial positions for IEEE journals and organized numerous international conferences. He has served on the SIAM Diversity Advisory Committee.

Dr. Win is an elected Fellow of the AAAS, the EURASIP, the IEEE, and the IET. He was honored with two IEEE Technical Field Awards: the IEEE Kiyo Tomiyasu Award (2011) and the IEEE Eric E. Sumner Award (2006, jointly with R. A. Scholtz). His publications, coauthored with students and colleagues, have received several awards. Other recognitions include the MIT Frank E. Perkins Award (2024), the MIT Everett Moore Baker Award (2022), the IEEE Vehicular Technology Society James Evans Avant Garde Award (2022), the IEEE Communications Society Edwin H. Armstrong Achievement Award (2016), the Cristoforo Colombo International Prize for Communications (2013), the Copernicus Fellowship (2011) and the *Laurea Honoris Causa* (2008) from the Università degli Studi di Ferrara, and the U.S. Presidential Early Career Award for Scientists and Engineers (2004).